

GRB 220831A: a hostless, intermediate Gamma-ray burst with an unusual optical afterglow

James Freeburn,^{1,2*} Brendan O’Connor,^{3†} Jeff Cooke,^{1,2} Dougal Dobie,^{2,4} Anais Möller,^{1,2} Nicolas Tejos,⁵ Jielai Zhang,¹ Paz Beniamini,^{6,7,8} Katie Auchettl,^{2,9,10} James DeLaunay,¹¹ Simone Dichiara,¹¹ Wen-fai Fong,¹² Simon Goode,^{2,13} Alexa Gordon,¹² Charles D. Kilpatrick,¹² Amy Lien,¹⁴ Cassidy Mihalenko,^{2,15} Geoffrey Ryan,¹⁶ Karelle Siellez,^{2,15} Mark Suhr,¹ Eleonora Troja¹⁷, Natasha Van Bemmell,^{1,2} and Sara Webb^{1,2}

¹Centre for Astrophysics and Supercomputing, Swinburne University of Technology, John St, Hawthorn, VIC 3122, Australia

²ARC Centre of Excellence for Gravitational Wave Discovery (OzGrav), John St, Hawthorn, VIC 3122, Australia

³McWilliams Center for Cosmology and Astrophysics, Department of Physics, Carnegie Mellon University, Pittsburgh, PA 15213, USA

⁴Sydney Institute for Astronomy, School of Physics, University of Sydney, Sydney, NSW 2006, Australia

⁵Instituto de Física, Pontificia Universidad Católica de Valparaíso, Casilla 4059, Valparaíso, Chile

⁶Department of Natural Sciences, The Open University of Israel, P.O. Box 808, Ra’anana 43537, Israel

⁷Astrophysics Research Center of the Open University (ARCO), The Open University of Israel, P.O. Box 808, Ra’anana 43537, Israel

⁸Department of Physics, The George Washington University, Washington, DC 20052, USA

⁹School of Physics, The University of Melbourne, Parkville, VIC 3010, Australia

¹⁰Department of Astronomy and Astrophysics, University of California, Santa Cruz, CA 95064, USA

¹¹Department of Astronomy and Astrophysics, The Pennsylvania State University, 525 Davey Lab, University Park, PA 16802, USA.

¹²Center for Interdisciplinary Exploration and Research in Astrophysics (CIERA) and Department of Physics and Astronomy, Northwestern University, Evanston, IL 60208, USA

¹³School of Physics and Astronomy, Monash University, VIC 3800, Australia

¹⁴Department of Physics and Astronomy, University of Tampa, 401 W. Kennedy Blvd, Tampa, FL 33606, USA

¹⁵School of Natural Sciences, University of Tasmania, Private Bag 37 Hobart, Tasmania, 7001, Australia

¹⁶Perimeter Institute for Theoretical Physics, Waterloo, Ontario N2L 2Y5, Canada

¹⁷University of Rome Tor Vergata, Department of Physics, via della Ricerca Scientifica 1, 00100, Rome, IT

Accepted XXX. Received YYY; in original form ZZZ

ABSTRACT

GRB 220831A is a gamma-ray burst (GRB) with a duration and spectral peak energy that places it at the interface between the distribution of long-soft and short-hard GRBs. In this paper, we present the multi-wavelength follow-up campaign to GRB 220831A and its optical, near-infrared, X-ray and radio counterparts. Our deep optical and near-infrared observations do not reveal an underlying host galaxy, and establish that GRB 220831A is observationally hostless to depth, $m_i \gtrsim 26.6$ AB mag. Based on the Amati relation and the non-detection of an accompanying supernova, we find that this GRB is most likely to have originated from a collapsar at $z > 2$, but it could also possibly be a compact object merger at $z < 0.4$ with a large separation distance from its host galaxy. Regardless of its origin, we show that its optical and near-infrared counterpart departs from the evolution expected from a forward shock dominated synchrotron afterglow, exhibiting a steep post-break temporal powerlaw index of $-3.83^{+0.62}_{-0.79}$, too steep to be the jet-break. By analysing a range of models, we find that the observed steep departure from forward shock closure relations is likely due to an internal process producing either a flare or a plateau.

Key words: transients: gamma-ray bursts – transients: neutron star mergers – stars: jets

1 INTRODUCTION

Gamma-ray bursts (GRBs) have a bimodal distribution in their observed duration and spectral hardness (Kouveliotou et al. 1993). From this phenomenon, GRBs are traditionally divided into two classes. Short-hard GRBs (SGRBs), with durations $\lesssim 2$ s, are associated with

binary neutron star (BNS) mergers (Eichler et al. 1989; Gehrels et al. 2005; Abbott et al. 2017) while long-soft GRBs (LGRBs), with durations $\gtrsim 2$ s, are associated with collapsars (Woosley 1993; Galama et al. 1998; Hjorth et al. 2003). However, the duration and hardness of the prompt γ -ray emission do not necessarily determine a progenitor for a specific event (Zhang et al. 2009). There are two reasons for this: Firstly, the distributions of SGRBs and LGRBs overlap significantly, preventing a secure classification of intermediate duration (~ 1 –3 s) GRBs. Secondly, there is an emerging population of GRBs, securely

* E-mail: jfreeburn@swin.edu.au

† McWilliams Fellow

in the LGRB distribution that are associated with mergers (Norris & Bonnell 2006).

The discovery of a supernova (SN) following the ~ 1 s duration, GRB 200826A (Ahumada et al. 2021; Zhang et al. 2021; Rossi et al. 2022) exemplified the overlap between the two distributions (e.g., Bromberg et al. 2012, 2013). Kilonovae (KNe) are associated with the r-process nucleosynthesis that occurs following the merger of two neutron stars. KNe were discovered associated with GRBs 211211A (Troja et al. 2022; Rastinejad et al. 2022; Yang et al. 2022; Mei et al. 2022; Gompertz et al. 2023) and 230307A (Levan et al. 2024; Sun et al. 2023; Yang et al. 2024; Gillanders et al. 2023; Dichiaro et al. 2023), despite being firmly in the LGRB distribution with durations in excess of 50 s (though see Barnes & Metzger 2023, for alternative explanations). These events cannot be explained merely in terms of scatter between the distributions of short and long duration GRBs, and conclusively demonstrate that the duration overlap between collapsars and mergers is larger than previously thought. The rest-frame $E_{\text{peak}}-E_{\text{iso}}$ correlation, often called the Amati relation, along with other similar empirical correlations (e.g., Guiriec et al. 2013; Golenetskii et al. 1983), can be used to partially distinguish the two populations (Amati et al. 2002; Amati 2006).

Distinguishing between GRB progenitors can be aided by the identification of a host galaxy and a redshift determination. LGRBs trace star formation and often reside in star forming galaxies coincident with their host’s stellar light distribution (Paczynski 1998; Bloom et al. 2002; Fruchter et al. 2006), whereas short GRBs are found in a variety of different galaxies (Leibler & Berger 2010; Fong & Berger 2013; Fong et al. 2013; Nugent et al. 2022) and generally reside at larger distances from the brightest parts of their host (Fong & Berger 2013; Fong et al. 2022; O’Connor et al. 2022a). Due to their differing redshift distributions and luminosities, arising from their distinct progenitor channels, the observed redshifts of these populations also differ significantly: LGRBs detected with *Swift* have a mean redshift of 2.8 (Jakobsson et al. 2006), whereas SGRBs have a lower mean redshift of ~ 0.6 (O’Connor et al. 2022a; Fong et al. 2022; Nugent et al. 2022).

GRB host galaxies can be difficult to identify and significant selection biases exist for both LGRBs (Krühler et al. 2015) and SGRBs at $z > 1$ (e.g., O’Connor et al. 2022a) due to the faintness of their host galaxies in this redshift range. Similarly, identifying some SGRB host galaxies can be complicated by a large angular offset, due potentially to natal kicks in the formation of BNS systems (Bloom et al. 2002; Berger 2010; Fong & Berger 2013; Behroozi et al. 2014; Beniamini & Piran 2024). It could also be due to long delay times between formation and merger, causing them to be associated with older and highly extended stellar populations in the host galaxy halos, that often remain unresolved (Perets & Beniamini 2021). Indeed, a large fraction of the SGRB population (~ 30 percent) do not have a spatially coincident host galaxy despite deep imaging (≥ 26 AB mag; Berger 2010; Tunnicliffe et al. 2014; O’Connor et al. 2022a). For those SGRBs with identified hosts, their progenitors have projected distances of tens of kpc from their host (Berger 2010; Fong & Berger 2013; O’Connor et al. 2022a; Fong et al. 2022).

GRB 220831A was a GRB detected by the Fermi Gamma-ray Burst Monitor (*Fermi*/GBM; Meegan et al. 2009) and the *Neil Gehrels Swift Observatory*’s Burst Alert Telescope (*Swift*/BAT; Gehrels et al. 2004) with a short duration (≤ 2 s) and a soft spectral profile (Wood et al. 2022; Tohuvavohu et al. 2022). This placed it in the intermediate region between SGRBs and LGRBs. The afterglow to GRB 220831A was detected at optical, near-infrared and radio wavelengths (Freeburn et al. 2022a; D’Avanzo et al. 2022; Anderson et al. 2022) and upper limits were placed in X-rays (Dichiaro et al.

2022). The optical and near-infrared afterglow was observed with the Dark Energy Camera (DECam), mounted on the Victor M. Blanco telescope, the *Gemini* South telescope, and the Very Large Telescope (VLT), yielding an unusually steep post-break temporal decay, which deviates from forward shock closure relations. GRB 220831A is similar in its properties to GRB 210704, which was an intermediate class burst, with a similarly difficult classification and deviations from a typical GRB afterglow (Becerra et al. 2023). Its peculiar properties highlight the importance of studying intermediate bursts like GRB 220831A.

In this work, we investigate GRB 220831A’s observational properties to shed light on its progenitor. In Section 2, we present observations of GRB 220831A’s prompt emission and afterglow, spanning from γ -ray to radio wavelengths. Without the identification of a host galaxy we evaluate the possible scenarios for GRB 220831A’s host in Section 3.1. We fit both empirical and forward shock models to the multi-wavelength observations of GRB 220831A. We then assess the deviations from canonical models by fitting the optical and near-infrared (OIR) data with an additional emission component in the form of either a flare or an internal plateau. This is presented in Section 3. We then conclude that the likely progenitor of GRB 220831A is a high- z collapsar and interpret the afterglow’s observed departures from closure relations in Section 4. Throughout this work we assume the cosmology reported in Planck Collaboration et al. (2020), report all uncertainties at the 1σ level and quote upper limits at the 5σ level.

2 DATA

2.1 High energy facilities

Fermi’s Gamma-ray Burst Monitor (GBM) detected GRB 220831A at 13:56:32.93 UT on 31 Aug 2022 (Wood et al. 2022), hereafter taken to be the start time, T_0 , of the GRB. We conducted analysis on the standard data products from the *Fermi*/GBM burst catalog (von Kienlin et al. 2020). GRB 220831A was visible only in five of the twelve NaI detectors (n_a , n_b , n_9 , n_8 and n_7) and neither of the BGO detectors that comprise *Fermi*/GBM. We calculate the T_{90} for GRB 220831A, defined by the difference in time between where 5 percent and 95 percent of GRB 220831A’s fluence is emitted (Kouveliotou et al. 1993). To do this, we utilise just the n_b detector, where the burst was brightest, and bin over 20–100 keV. We simulate a range of bursts based off the error associated with each time bin and generate a distribution of T_{90} values to yield $T_{90} = 1.83^{+0.50}_{-0.10}$ s. We performed a spectral analysis of the burst, from the five NaI detectors in which it is visible, using the *Fermi* Gamma-ray Data Tools package (Goldstein et al. 2023) between 4–100 keV and binning between $T_0 - 1.5$ s and $T_0 + 1.5$ s. The burst is best-fit with a Band function, with the peak spectral energy, $E_{\text{peak}} = 64^{+19}_{-14}$ keV, the low energy photon index, $\alpha_\gamma = -1.46^{+0.06}_{-0.07}$ and the high energy photon index, $\beta_\gamma = -3.8^{+6.2}_{-1.8}$. We place these properties in the context of other *Fermi*/GBM detected GRBs in the *Fermi*/GBM Gamma-ray Burst Spectral Catalog (Poolakkil et al. 2021) in Figure 1 and analyse these results in Section 3.2.

Swift/BAT was not successfully triggered on-board by GRB 220831A. No prompt alerts were provided by *Fermi*/GBM due to communication issues. With no prompt alert, the Gamma-Ray Urgent Archiver for Novel Opportunities (GUANO; Tohuvavohu et al. 2020), a pipeline used to archive *Swift*/BAT event data around times of interest, was unable to be triggered. Fortunately, there was a spurious transient ~ 5 s prior to the trigger time that tripped one of

Swift/BAT’s many rate trigger algorithms. When no point source was found in the on-board image, this trigger was classified as a “failed” trigger, which *Swift*/BAT archives 10 s of event data. The 10 s cover 7.7 s prior to the trigger time to 2.4 s after trigger, including the full prompt emission period of the burst. The spurious transient is separated temporally from the burst emission and did not affect the analysis of the burst. Using these event data the *Swift*/BAT-GUANO team was able to create a sky image and localize this burst with an uncertainty of $2'$ (Tohuvavohu et al. 2022). The initial analysis of the burst placed the measured duration of T_{90} at ~ 1 s (Tohuvavohu et al. 2022), placing it in the SGRB regime (Kouveliotou et al. 1993). Using the *Swift*/BAT tools in the HEASOFT (Heasarc 2014) software package, a spectral file was created from the event data over the full emission period of the burst (0.47 s prior to trigger time to 1.13 s after trigger time), as well as a detector response matrix. We fit the data with XSPEC (Arnaud 1996) and found $E_{\text{peak}} = 62 \pm 46$ keV from a Band function fit. Using the BATTBLOCKS tool we found a $T_{90} = 1.3 \pm 0.3$ s.

2.2 *Swift* Follow-up Observations

The X-ray Telescope (XRT) on-board *Swift* observed GRB 220831A starting on 1 November 2022 at 04:09:52 UT, corresponding to 0.6 d after the initial *Fermi* trigger. Dichiaro et al. (2022) report a low-significance detection at the location of the OIR afterglow (see Section 2.3). To quantify the presence of X-ray emission, we reduce the two observations associated with this event (ObsID: 00021512001 and 00021512002). We reprocessed all observations from level one XRT data using XRTPIPELINE version 0.13.7. Here we use the most recent calibrations files and standard filter and screening criteria¹. Using a source region with a radius of $49''$ centered on the position of GRB 220831A and a source-free background region with a radius of $120''$ centered at $(\alpha, \delta) = (01:37:11.2426, -41:31:30.093)$, we found no significant ($>3\sigma$) X-ray emission associated with individual observations that covered the GRB. To increase the signal to noise of our observations, we merged the two individual *Swift* observations using XSELECT version 2.5b. Similarly, we detected no X-ray emission associated with the position of the GRB 220831A, with a 0.3–10 keV 5σ upper limit of 0.002 counts s^{-1} . This suggests the possible detection by Dichiaro et al. (2022) was spurious. Assuming an absorbed powerlaw with a column density of $N_H = 1.59 \times 10^{20}$ cm^{-2} , a spectral index, β , of -0.69 , measured from a fit to the OIR afterglow in Section 3.3.1 and a redshift of 2.4 (see Section 3.1), we derive a 5σ upper limit to the flux of 4.43×10^{-13} $\text{erg cm}^{-2} \text{s}^{-1}$.

The Ultra-violet and Optical Telescope (UVOT) on-board *Swift* provided simultaneous observations to XRT. Klingler (2022) reported an upper limit of >23.4 AB mag with the UVOT *white* filter at ~ 18 h post-burst.

2.3 Optical and near-infrared observations

Here we summarize the deep OIR observations of GRB 220831A aimed at both its initial afterglow (Table 1) and late-time searches for its host galaxy (Table 2). These include observations with VLT, DECam, and 11.1 hr of Gemini-South observations across multiple programs.

GRB 220831A’s OIR counterpart was discovered at $(\alpha, \delta) = (01:37:00.95, -41:35:34.37)$, 19.4 h post-burst with VLT/HAWK-I follow-up (PI: Tanvir, D’Avanzo et al. 2022).

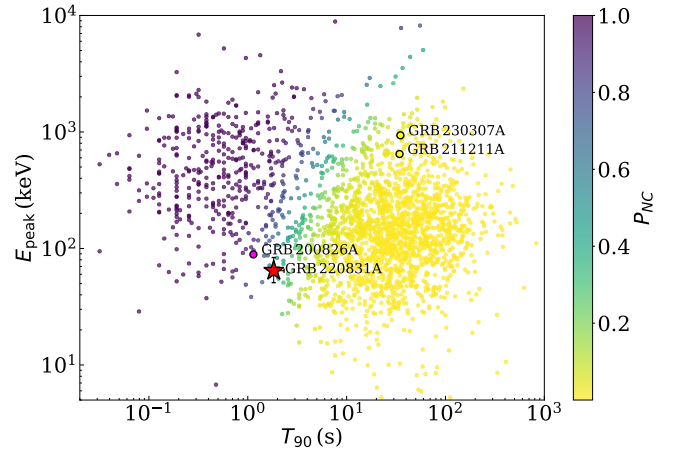


Figure 1. T_{90} versus the observer frame spectral peak energy, E_{peak} from the *Fermi*-GBM Gamma-Ray Burst Spectral Catalog (Poolakkil et al. 2021) fit with the Band function (Band et al. 1993). We fit the distribution with two Gaussian distributions in log-space. Based on this fit, each GRB is colour-coded with the probability of it being a non-collapsar, P_{NC} (e.g., Bromberg et al. 2013), where yellow and purple denote a 0 and 100 percent probability of being a non-collapsar respectively.

Subsequently, the optical counterpart was observed using DECam between 1 November 2022 and 4 November 2022, corresponding to 0.6 d and 3.8 d post-burst respectively (PI: Cooke, Freeburn et al. 2022a,b). An additional two epochs of VLT observations with FORS2 and HAWK-I were conducted at 1.7 d and 2.8 d post-burst. Later, the optical counterpart was observed with Gemini/GMOS at 4.6 d post-burst (PI: Gordon, Gordon et al. 2022) in *r* and *i* filters, revealing a steep temporal break in the OIR light curve.

Gemini/FLAMINGOS-2 near-infrared observations (PI: O’Connor) were carried out in the *J* and *K_s* filters at 9, 10 and 52 d post-burst. These data appeared to show a near-infrared source (O’Connor et al. 2022b), spatially coincident with the OIR afterglow with a brightness of ~ 24.5 AB mag and 23.5 AB mag, respectively. However, the counterpart, detected with *Gemini*/FLAMINGOS-2, had a small angular offset from the previous OIR afterglow observations of $\sim 0.6''$ (see Figure A1 and Appendix A). Moreover, VLT/HAWK-I observations at ~ 9 d post-burst, shortly after the initial *Gemini* epoch, yielded an upper limit of $J \gtrsim 24.9$ AB mag, which conflicts with the brightness of the multi-epoch *Gemini* *J*-band detections. Based on a detailed re-analysis of all of the *Gemini* OIR data, we conclude that the near-infrared detections were spurious and likely due to an unknown image artefact caused by residuals from the sky subtraction combined with the dither pattern (Kathleen Labrie, private communication). The artefact was not present in the late-time (July 2023) *J*-band *Gemini* observations discussed below. A more detailed analysis of these observations is included in Appendix A.

After the OIR counterpart to GRB 220831A had faded, the field was subsequently observed using VLT HAWK-I and FORS2 instruments and provided upper limits at 5.7, 8.7, 22.6 and 26.8 days post-burst in the *R*, *J*, *R*, and *J* filters, respectively (PI: Tanvir, D’Avanzo et al. 2022). It was also observed by *Gemini*/GMOS at 24.5 d post-burst in *Z*-band (PI: O’Connor). Further late-time, deep observations were conducted with *Gemini* in *J*-band in July 2023 (PI: O’Connor) and in the *g*, *i*, *J* and *K_s* filters between December 2023 and March 2024 (PI: Tejos). These observations did not reveal any likely host galaxy coincident with the subarcsecond OIR afterglow localization.

¹ http://swift.gsfc.nasa.gov/analysis/xrt_swguide_v1_2.pdf

The upper limits on an angularly coincident host galaxy are provided in Table 2.

The photometric measurements presented in Tables 1 and 2 were conducted with aperture photometry using SOURCE EXTRACTOR (Bertin & Arnouts 1996). For filters g , R , r , i , I and Z , the photometric catalogue from the Dark Energy Survey’s second data release (Abbott et al. 2021) was used for calibration with Lupton transformations² for R and I .

2.4 Radio observations

GRB 220831A was observed with the Australia Telescope Compact Array (ATCA) at 4 and 11 d post-burst by an independent group (PI: Anderson, Anderson et al. 2022). Both observations were carried out using the 4 cm receiver, with two 2048 MHz continuum bands centered on 5.5 and 9 GHz. We have calibrated and imaged the publicly available data from both observations using the standard MIRIAD techniques. We report a marginal detection of $55 \pm 15 \mu\text{Jy}$ at 9 GHz in the second observation, but no detections otherwise (see Table 1 for details).

3 MULTI-WAVELENGTH ANALYSIS

3.1 A deep search for the host galaxy

Despite deep follow-up observations with VLT and *Gemini*, we do not detect a host galaxy within $2''$ of the subarcsecond localization of GRB 220831A to ≥ 26 AB mag (Table 2). Therefore, we expand our search for a host galaxy to larger angular distances.

3.1.1 NGC 625

NGC 625 has an angular separation of $23.7'$ from GRB 220831A and has a measured distance of 3.89 ± 0.39 Mpc from Earth (Karachentsev & Kashibadze 2006). GRB 220831A would therefore lie 26.8 ± 2.7 kpc from NGC 625 in projection, well within observed projected separations for SGRBs (O’Connor et al. 2022a; Fong et al. 2022). However, this would make GRB 220831A the closest GRB ever discovered, whereas the brightness of its prompt emission would imply $E_{\gamma,\text{iso}} = 1.23^{+0.32}_{-0.20} \times 10^{45}$ erg, which is significantly less energetic than the observed, on-axis GRB population. At such a nearby distance, the continued deep monitoring by *Gemini* and VLT would have uncovered either a clear KN, assuming a brightness similar to AT2017gfo (Smartt et al. 2017; Pian et al. 2017; Evans et al. 2017; Covino et al. 2017; Abbott et al. 2017; Tanvir et al. 2017; Andreoni et al. 2017), or SN in excess of the afterglow (see Section 3.4). The lack of these features implies a much larger distance than 4 Mpc.

A magnetar giant flare (MGF) would be consistent with the isotropic-equivalent gamma-ray energy release at this distance and the lack of KN and SN detection. Observations of Galactic magnetars show they are predominantly confined to the thin disk (Kaspi & Beloborodov 2017). GRB 220831A’s location 26.8 ± 2.7 kpc from NGC 625 would be strange for a magnetar and inconsistent with their magnetic field decay times of $10^3 - 10^4$ yr (Colpi et al. 2000; Beniamini et al. 2019). We therefore conclude that NGC 625 is an unlikely host galaxy for GRB 220831A.

² <http://www.sdss3.org/dr8/algorithms/sdssUBVRITransform.php>

Table 1. Observations of GRB 220831A’s afterglow.

Instrument	Band	Time Days after GRB	Flux Density μJy	Ref.
<i>Swift</i> / XRT	1 keV	0.75	< 0.096	1
<i>Swift</i> / UVOT	<i>white</i>	0.75	< 1.6	2
<i>Blanco</i> / DECAM	<i>g</i>	0.8	1.39 ± 0.19	3,4
	<i>r</i>	0.8	1.94 ± 0.14	
	<i>i</i>	0.8	2.17 ± 0.18	
	<i>g</i>	1.6	0.82 ± 0.18	
	<i>r</i>	1.6	0.90 ± 0.13	
	<i>i</i>	1.6	1.22 ± 0.11	
	<i>g</i>	1.8	< 0.96	
	<i>r</i>	1.8	0.93 ± 0.14	
	<i>i</i>	1.8	1.09 ± 0.12	
	<i>i</i>	3.8	< 0.62	
VLT/ HAWK-I	<i>J</i>	0.8	2.75 ± 0.23	5
	<i>J</i>	1.7	1.500 ± 0.097	
	<i>J</i>	2.7	0.85 ± 0.11	
	K_s	2.8	1.23 ± 0.16	
	<i>J</i>	26.8	< 0.74	
VLT/ FORS2	<i>R</i>	2.7	0.331 ± 0.022	
	<i>I</i>	2.7	0.501 ± 0.044	
	<i>R</i>	22.6	< 0.21	
ATCA	9 GHz	4.1	< 70	6
	5.5 GHz	4.1	< 70	
	9 GHz	11.2	55 ± 15	
	5.5 GHz	11.2	< 45	
<i>Gemini</i> / GMOS	<i>r</i>	4.6	< 0.12	7
	<i>i</i>	4.6	0.109 ± 0.031	
	<i>Z</i>	57.4	< 0.58	

References. (1) Dichiara et al. (2022); (2) Klingler (2022); (3) Freeburn et al. (2022a); (4) Freeburn et al. (2022b); (5) D’Avanzo et al. (2022); (6) Anderson et al. (2022); (7) Gordon et al. (2022).

Table 2. Brightness constraints on a host galaxy spatially coincident with GRB 220831A.

Instrument	Band	m	M at $z = 2.4$
<i>Gemini</i> /GMOS	<i>g</i>	> 26.2	> -19.0
	<i>r</i>	> 26.2	> -19.0
	<i>i</i>	> 26.5	> -18.7
	<i>Z</i>	> 24.5	> -20.7
VLT/FORS2	<i>R</i>	> 25.6	> -19.6
VLT/HAWK-I	<i>J</i>	> 24.9	> -20.3
<i>Gemini</i> /FLAMINGOS-2	<i>J</i>	> 24.6	> -20.6
	K_s	> 24.0	> -21.2

3.1.2 Other field galaxies

Bloom et al. (2002) calculate the probability of a transient being coincident with a given galaxy by chance, $P_{\text{cc,gal}}$, using,

$$P_{\text{cc,gal}} = 1 - \exp[-\pi r_{\text{gal}}^2 \sigma(\leq m_{R,\text{gal}})] \quad (1)$$

where r_{gal} is the angular separation between the event and a given galaxy, σ is the number density of galaxies at or brighter than the apparent magnitude, $m_{R,\text{gal}}$, of the candidate host galaxy in R -band. In what follows, we utilize this probability of chance coincidence to test the likelihood of association for the surrounding galaxies in our deep imaging.

Following O’Connor et al. (2022a), we consider a one arcminute radius from GRB 220831A’s OIR sub-arcsecond afterglow localization in *Gemini*/GMOS i -band imaging. This is because, for the vast majority of SGRBs, a confident host galaxy association has not been possible beyond a separation of $1'$. We identify potential host galaxies by using our deep r and i -band *Gemini*/GMOS imaging and calculating an R -band magnitude with a Lupton transformation. We then select those that have a 5σ detection, satisfy $P_{\text{cc,gal}} < 0.99$ and a cut using SOURCE EXTRACTOR’s star-galaxy classifier, CLASS_STAR < 0.5 . The resultant selection of galaxies are shown in Figure 2. The position of these galaxies, in addition to their R -band AB magnitudes, photometric redshifts and projected physical offsets, are also listed in in Table 3. We find that G1, at an angular offset of $16.5''$, has the lowest probability of chance coincidence at $P_{\text{cc,gal}} = 0.42$, which is a very unlikely host for GRB 220831A. However, of the galaxies with measured photometric redshifts listed in Table 3, G1, G3 and G4 have separations that are consistent with the observed separation distances of SGRB host galaxies, which range up to ~ 75 kpc (O’Connor et al. 2022a; Fong et al. 2022). While we cannot rule out the low- z SGRB scenario, we disfavour it based on the lack of significant association with any of the galaxies shown in Table 3. In addition, because we find no coincident host galaxy down to the depths listed in Table 2, we therefore conclude that GRB 220831A’s host galaxy is not present in our observations.

3.1.3 An unseen host galaxy

LGRBs are usually confined to star formation regions within their host galaxies (Bloom et al. 2002; Paczyński 1998). A high- z host not detected to the absolute magnitude limits shown in Table 2 lies in the $\sim 80^{\text{th}}$ percentile of the brightness of observed LGRB host galaxies for $1.9 < z < 2.7$ (Schulze et al. 2015). For GRB 220831A, this would imply a range of $2.11 \times 10^{51} \text{ erg} < E_{\gamma,\text{iso}} < 5.49 \times 10^{51} \text{ erg}$. This, along with its location on the Amati relation in Figure 3, favours a faint, high- z host underlying the position of GRB 220831A that is not detected in our deep ground-based imaging.

3.2 The prompt emission

Here we consider the prompt emission properties of GRB 220831A in order to aid in determining its nature as either an SGRB or LGRB. To start, we fit the distribution of bursts from the *Fermi*-GBM Gamma-Ray Burst Spectral Catalog (Poolakkil et al. 2021) in T_{90} - E_{peak} space with a two-dimensional bimodal distribution. Figure 1 shows that GRB 220831A occupies an intermediate region in T_{90} - E_{peak} space between SGRBs and LGRBs. Based on our fitted distributions and the *Fermi*/GBM of GRB 220831A, we obtain $P_{\text{NC}} = 0.54^{+0.10}_{-0.23}$. Moreover, from the *Fermi*/GBM data, with the procedure described in Bromberg et al. (2013), we calculate the probability of GRB 220831A being a non-collapsar as $P_{\text{NC}} = 0.48^{+0.12}_{-0.34}$. These two methods are in agreement. Therefore, using the observer frame prompt emission properties alone, we cannot discern its nature due to its intermediate position in Figure 1.

With the rest-frame spectral peak energy and the γ -ray, isotropic-equivalent energy release, $E_{\text{rest,peak}}-E_{\gamma,\text{iso}}$, the Amati relation can

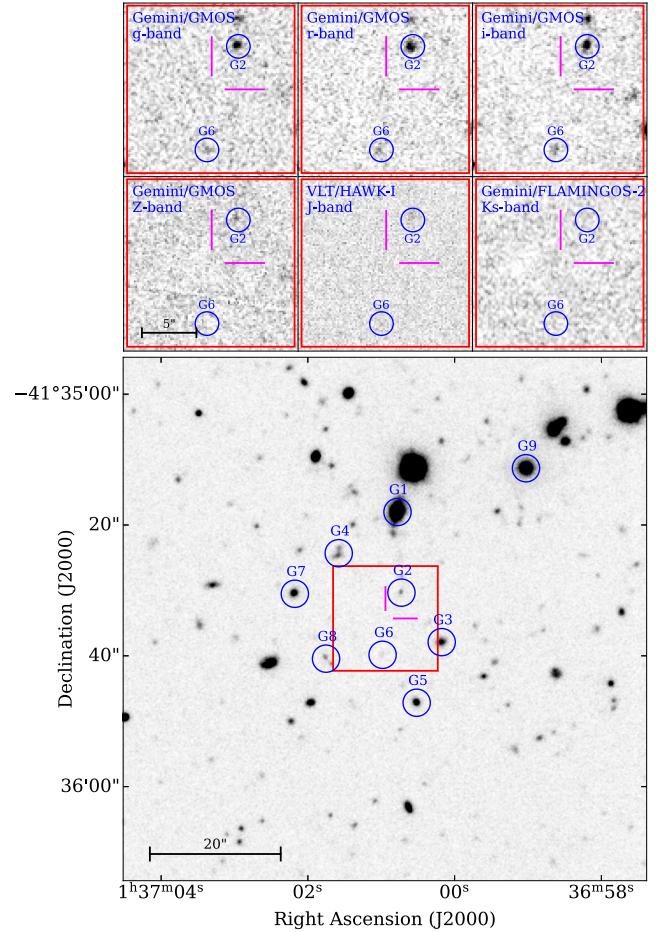


Figure 2. The bottom panel shows a *Gemini*/GMOS i -band image of the field surrounding GRB 220831A’s OIR afterglow with 5σ depth of 26.5 AB mag. The location of GRB 220831A’s OIR afterglow is marked with the magenta cross hairs and galaxies within 1 arcminute with $P_{\text{cc,gal}} < 0.99$ are marked with blue circles and labelled G1-8. Their properties are listed in Table 3. There was no photometric redshift available for G2, G6 and G8. The top panel shows the $16''$ red box in the top plot, zoomed in and shown in different filters with which deep imaging was conducted. The limits of these images are shown in Table 2.

be used to infer the likely progenitor of a given GRB (Amati et al. 2002; Amati 2006). However, without a redshift, we cannot calculate the rest frame properties of GRB 220831A.

Assuming a collapsar scenario for GRB 220831A, we can use the $E_{\text{rest,peak}}-E_{\gamma,\text{iso}}$ correlation to calculate the redshift at which the emission properties of GRB 220831A pass closest to the Amati relation (see Figure 3). This is called the ‘pseudo-redshift’ (Amati 2006) and we calculate a value of $z = 2.4$. Similarly, for $z < 0.4$, GRB 220831A is consistent with the SGRB Amati relation to within 3σ in $E_{\text{rest,peak}}-E_{\gamma,\text{iso}}$ space. G1 and G4 in Table 3 are consistent with this redshift range.

3.3 The afterglow

3.3.1 Observed properties

The OIR data, shown in Figure 4, shows a clear temporal break before the last epoch of *Gemini*/GMOS observations. We fit the OIR and

Table 3. Host galaxy candidates for GRB 220831A.

Label	Coordinates	$m_{R,gal}$ AB mag	Angular Separation "	$P_{cc,gal}$	z_{phot}	Projected Distance kpc
G1	01:37:00.8 -41:35:18.0	21.452 ± 0.011	16.5	0.42	0.23 ± 0.13	61^{+22}_{-22}
G2	01:37:00.7 -41:35:30.3	24.585 ± 0.064	4.8	0.43	–	–
G3	01:37:00.2 -41:35:37.9	23.660 ± 0.036	9.3	0.69	0.89 ± 0.23	72^{+4}_{-8}
G4	01:37:01.6 -41:35:24.3	23.870 ± 0.039	12.3	0.83	0.77 ± 0.49	93^{+12}_{-40}
G5	01:37:00.5 -41:35:47.1	23.375 ± 0.029	13.6	0.84	0.86 ± 0.30	107^{+8}_{-17}
G6	01:37:01.0 -41:35:39.9	25.91 ± 0.19	5.9	0.89	–	–
G7	01:37:02.2 -41:35:30.3	23.792 ± 0.044	14.4	0.89	1.07 ± 0.16	120^{+3}_{-5}
G8	01:37:01.8 -41:35:40.4	24.870 ± 0.083	10.4	0.95	–	–
G9	01:36:59.0 -41:35:11.3	22.199 ± 0.017	31.5	0.97	0.85 ± 0.06	245^{+5}_{-6}

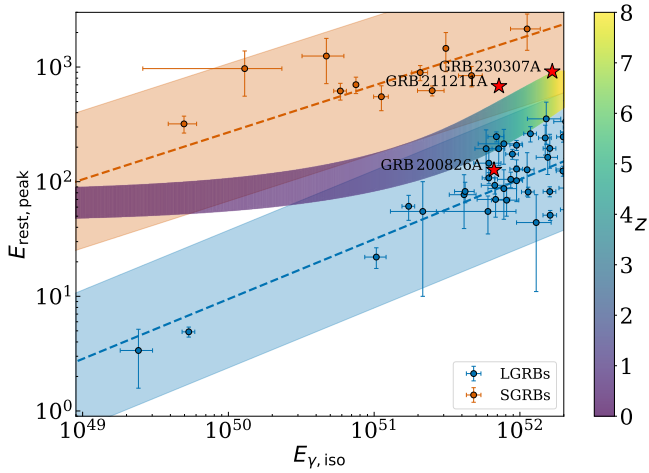


Figure 3. GRB 220831A and a selection of SGRBs and LGRBs plotted in rest-frame $E_{rest,peak}-E_{\gamma,iso}$ space compared to the Amati relation (adapted from [Dichiara et al. 2021](#)). The Amati relation for SGRBs (orange) and LGRBs (blue) is plotted with a dotted line with a filled, shaded region denoting the 3σ scatter in the correlation. We plot GRB 220831A’s location in $E_{rest,peak}-E_{\gamma,iso}$ space for $0 < z < 8$, where the colour bar denotes z .

Swift/XRT data with a broken powerlaw (BPL) of the form,

$$F(\nu, t) = A\nu^\beta \begin{cases} (t/t_b)^{\alpha_1}, & t < t_b \\ (t/t_b)^{\alpha_2}, & t > t_b \end{cases} \quad (2)$$

where A is the flux density scaling factor, t is the time post-burst in days, t_b is the time post-burst of a break in the temporal powerlaw index, ν is frequency, β is the spectral index of the afterglow emission and α_1 and α_2 are the pre and post-break temporal powerlaw indices.

We explore the parameter space using `EMCEE` ([Foreman-Mackey et al. 2013](#)). This yielded the following results; $t_b = 2.60^{+0.10}_{-0.11}$ d, $\alpha_1 = -0.89^{+0.07}_{-0.07}$, $\alpha_2 = -3.83^{+0.62}_{-0.79}$ and $\beta = -0.64^{+0.07}_{-0.07}$ with a reduced χ^2 value of 0.75. We therefore conclude that the afterglow data is consistent with a constant spectral index and a dramatic steepening of the fade rate between approximately 2 and 4 days post-burst.

Under the standard afterglow model wherein synchrotron emission results from a relativistic shock interacting with a uniform interstellar medium and observing the afterglow between the typical frequency

and the cooling frequency, $\nu_m < \nu < \nu_c$, the electron energy distribution powerlaw index, p , predicts values of $\alpha = 3(1-p)/4$, $\beta = (1-p)/2$ for the pre-break light curve ([Sari et al. 1998](#)). Due to the lateral spreading of the jet, there is expected to be a steepening in the fade rate of the afterglow emission. This is called the ‘jet-break’ and is characterised by the temporal powerlaw index, α , asymptoting to $-p$ ([Rhoads 1997](#); [Panaitescu & Mészáros 1999](#)).

From the pre-break values of β and α_1 , we calculate $p = 2.22 \pm 0.07$ ([Granot & Sari 2002](#)). This pre-break behavior, in terms of both temporal and spectral index, is consistent with the standard closure relations. However, if we interpret the sharp temporal break as a jet-break, the fitted value of $\alpha_2 = -3.83^{+0.62}_{-0.79}$, is inconsistent with this prescription with a significance of 3.6σ , calculated from the posterior distribution shown in [Figure 5](#). Furthermore, it is not possible to generate such a decay with a forward shock. The steepest decay possible would be limited by high altitude emission, resulting in $\alpha_2 = -2 + \beta$ ([Kumar & Panaitescu 2000](#)). It also constitutes an outlier in the distribution of observed temporal powerlaw indices, which is shown in [Figure 6](#) ([Wang et al. 2018](#)). Therefore, our inferred value of α_2 is too steep to originate from a forward shock alone. GRB 060605 has a similarly steep post-break temporal powerlaw index ([Ferrero et al. 2009](#)), which can be seen in [Figure 6](#). This will be discussed in [Section 3.4](#) and [Section 4](#).

3.3.2 Preliminary afterglow modeling

In [Figure 4](#), we fit GRB 220831A’s afterglow light curve using `AFTERGLOWPY`, a `PYTHON` package for generating synthetic afterglow light curves from numerical forward shock models. We assume a uniform density circumburst medium and a top-hat jet model with an on-axis viewing angle of 0° . We assume a top-hat as the presence of any angular structure would result in a shallower post-break light curve, leading to a larger discrepancy between forward shock models and our observations (e.g., [Ryan et al. 2020](#); [Beniamini et al. 2020b, 2022](#)). We fit the data with the Bayesian inference library, `BILBY` ([Ashton et al. 2019](#)), with the nested sampler, `DYNESTY` ([Speagle 2020](#)).

Due to GRB 220831A’s unconstrained progenitor and degeneracies in the redshift solution based on the Amati relation (see [Figure 3](#)), we explore both a high ($z = 2.4$) and low ($z = 0.2$) redshift in our afterglow modelling. Known degeneracies in $E_{K,iso}$, n_0 and z result in similar fits to the data. As we favour a high- z , collapsar scenario, we assume $z = 2.4$ for the remainder of this work, but present the

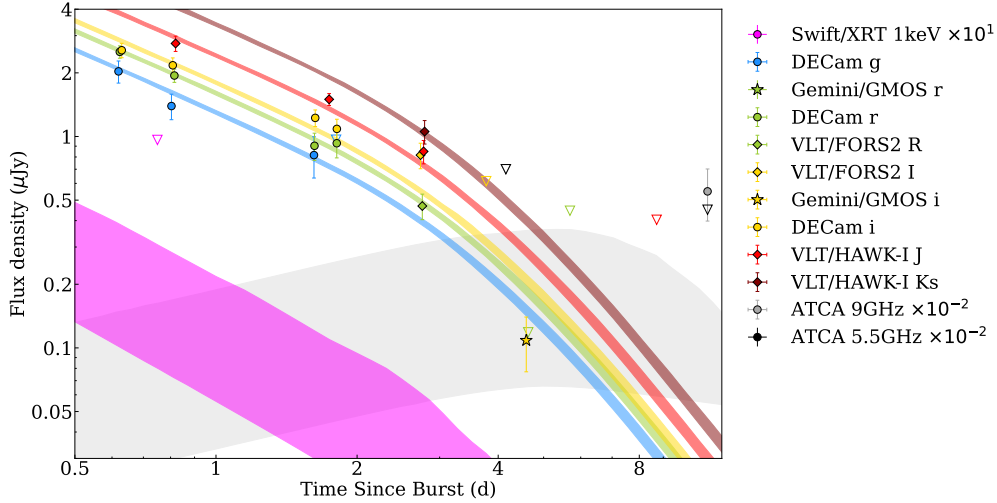


Figure 4. The light curve of GRB 220831A’s afterglow. The shaded regions show the 1σ intervals for the multi-wavelength, forward shock fit AFTERGLOWPY (Ryan et al. 2020) model, assuming $z = 2.4$ (the first row in Table 4). The X-ray and radio data and models have been rescaled for clarity.

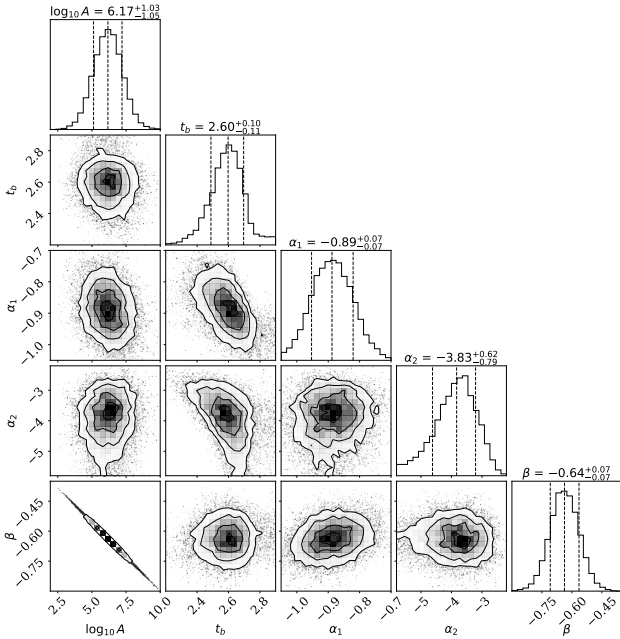


Figure 5. Corner plot of the phenomenological BPL fit to the afterglow of GRB 220831A. The α_2 value constitutes a 3.6σ tension with the post-break value predicted from closure relations, assuming the observed temporal break is the jet-break.

result of the fits to the afterglow data, assuming $z = 0.2$, in Appendix B.

We fit all of the available data presented in Table 1 for $E_{K,iso}$, the jet-opening angle, θ_j , p , the number density of the circumburst medium, n_0 and the forward shock’s energy fraction stored in the electrons and the magnetic field, ϵ_e and ϵ_B respectively. The resultant fit is shown in Figure 4 and the median of the posterior distribution has $\chi^2_{red} = 33.47$. Given that our BPL fit to the OIR data yielded a value of α_2 that was unusually steep it is unsurprising that the AFTERGLOWPY fails to simultaneously predict the post-break *Gem-*

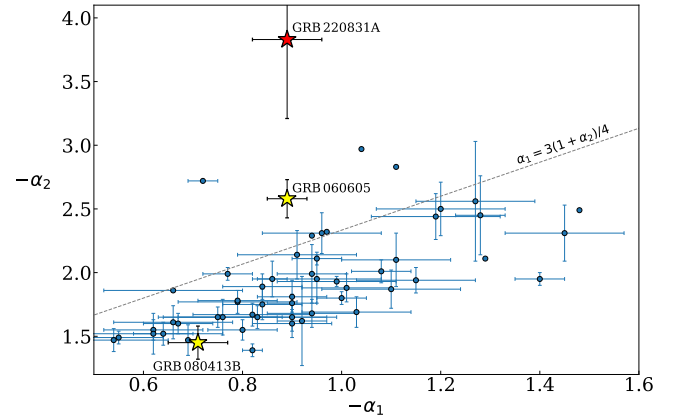


Figure 6. Temporal powerlaw indices for the sample of GRB afterglows analysed in Wang et al. (2018). We also plot GRB 220831A’s location in parameter space and the predictions from forward shock closure relations, assuming a uniform circumburst density and $v_m < v < v_c$, denoted by the grey dotted line. In the Wang et al. (2018) sample, the afterglows of GRBs 060605 and 080413B are plotted, both of which had a possible OIR internal plateau (Li et al. 2012). The values of α_1 and α_2 for GRB 060605 are taken from Ferrero et al. (2009).

ini/GMOS *i*-band detection and *r*-band upper limit at 4.6 d post-burst and the pre-break OIR detections, particularly the VLT observations at ~ 2.7 d post-burst. The best-fit model also underpredicts the observed flux density at 9 GHz at approximately 11 days post-burst. At this observing frequency, scintillation-induced extrinsic variability may be as high as 100% (see Dobie et al. 2020, and references therein). With only one detection we cannot determine whether the observed flux density is representative of the intrinsic luminosity of the source, or whether it appears substantially brighter by chance. Alternatively it also could be due to the shortcomings of current forward shock models in simultaneously modeling X-ray, OIR and radio afterglows (e.g., Marongiu et al. 2022). The parameter estimations from the resultant fit is shown in Table 4.

Table 4. Forward shock parameter estimations from AFTERGLOWPY fits of GRB 220831A’s afterglow assuming $z = 2.4$. ϵ_γ denotes the γ -ray efficiency of a given model and χ^2_{red} is the reduced χ^2 statistic for each model’s fit to the data. The corner plots associated with these fits are shown in Appendix C.

Data	Fit	$E_{K,\text{iso}}$ \log_{10} erg	n_0 \log_{10} cm $^{-3}$	θ_j rad	p	$\log_{10} \epsilon_e$	$\log_{10} \epsilon_B$	ϵ_γ	χ^2_{red}
All	Forward shock	$52.51^{+0.76}_{-0.79}$	$-2.43^{+1.13}_{-0.98}$	$0.06^{+0.02}_{-0.02}$	$2.27^{+0.06}_{-0.06}$	$-0.66^{+0.51}_{-0.47}$	$-1.85^{+1.17}_{-1.61}$	$0.10^{+0.36}_{-0.09}$	33.47
OIR	Forward shock	$52.07^{+0.39}_{-0.12}$	$-1.97^{+0.24}_{-1.16}$	$0.07^{+0.01}_{-0.03}$	$2.25^{+0.06}_{-0.06}$	-1	-1	$0.26^{+0.10}_{-0.16}$	3.24
OIR	Forward shock + flare	$52.18^{+0.18}_{-0.16}$	$-2.41^{+0.52}_{-0.49}$	$0.06^{+0.01}_{-0.01}$	$2.27^{+0.07}_{-0.07}$	-1	-1	$0.21^{+0.11}_{-0.10}$	2.00
OIR	Forward shock + internal plateau	$52.05^{+0.19}_{-0.21}$	$-2.75^{+0.56}_{-0.60}$	$0.05^{+0.01}_{-0.01}$	$2.27^{+0.07}_{-0.07}$	-1	-1	$0.27^{+0.15}_{-0.12}$	1.11

3.4 Possible secondary emission components

The deviations from the standard closure relations (see Section 3.3) could be explained by invoking a separate emission component, dominating between approximately one and three days post-burst. Here we consider a few of the possible interpretations. As we cannot directly associate GRB 220831A to a progenitor class (collapsar versus merger; see Section 3.2) we consider both *i*) a SN excess in Section 3.4.1, and *ii*) a KN excess in Section 3.4.2. We further consider two progenitor independent mechanisms: *iii*) a delayed flare in Section 3.4.3 and *iv*) an internal plateau in Section 3.4.4.

3.4.1 Supernova

LGRBs at low redshifts are typically found to have produced observable SN (Hjorth 2013; Cano et al. 2017). The GRB-SN light curves peak at >10 d post-burst in the rest-frame (Hjorth 2013; Cano et al. 2017), which would result in a shallower observed value of α_2 compared to a forward shock, which is the opposite of what we observe.

However, we can still use our sensitive OIR observations occurring out to 57 days post-burst, shown in Table 1, to constrain the presence of a SN accompanying GRB 220831A. We use a synthetic grid of light curves based on SN 1998bw, the SN accompanying GRB 980425 (Galama et al. 1998), using the model described in Levan et al. (2005) with the SNCosmo library (Barbary et al. 2024). The *R*-band 5σ upper limit of $m_R > 25.6$ AB mag at 23 days post-burst is most constraining for the existence of an SN and rules out synthetic light curves with $z \lesssim 0.9$ (see Figure 7). This is consistent with the non-detection of an obvious host galaxy, which also implies a higher redshift (see Section 3.1).

3.4.2 Kilonova

If there was detectable KN emission associated with GRB 220831A, we would expect reddening similar to that observed in other KNe. However, the observed data prior to the temporal break is consistent with a constant spectral index, β . Moreover, the steep decay of the *i*-band light curve would suggest the potential for a separate emission component that decays faster than the afterglow. This evolution is not expected for KNe and was not observed in the KN accompanying GW170817, AT2017gfo (Smartt et al. 2017; Pian et al. 2017; Evans et al. 2017; Covino et al. 2017; Abbott et al. 2017; Tanvir et al. 2017; Andreoni et al. 2017), which decayed slower in *i*-band than typical, on-axis afterglow emission. Moreover, the lack of an obvious low- z host disfavors a distance from which a KN would be detectable. We

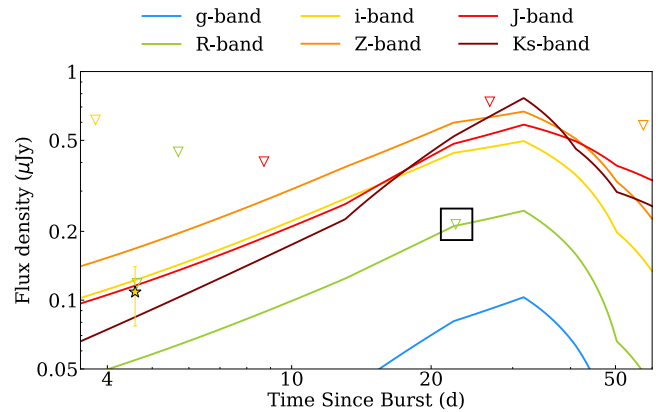


Figure 7. Model SN light curve based on observations of SN 1998bw (Levan et al. 2005; Barbary et al. 2024), shifted to $z = 0.86$. We also show observations of GRB 220831A’s OIR counterpart out to 57 d post-burst which are listed in Table 1. In this scenario, the SN emission would dominate the Gemini/GMOS *i*-band detection of the OIR counterpart at 4.6 d post-burst and would be just below the VLT/FORS2 upper limit of $m_R > 25.6$ AB mag at 23 d post-burst, which is highlighted in the plot with a black square.

therefore conclude that the presence of a KN in our observations is unlikely.

3.4.3 Flare

Most X-ray and optical afterglows, exhibit some flaring activity (Li et al. 2012; Swenson et al. 2013; Swenson & Roming 2014). These flares are morphologically varied and have a range of different explanations. Some can be explained by energy injection into the forward shock (Burrows et al. 2005; Romano et al. 2006; Falcone et al. 2006), although many other explanations exist (e.g., Dai et al. 2006; Perna et al. 2006; Duque et al. 2022). In the case of GRB 220831A, the steep, post-break, powerlaw index would suggest an internal process over energy injection into the forward shock. Optical flares like this have been observed before such as the optical afterglows to GRB 070311 and GRB 071010A (Li et al. 2012). Explanations for these flares include time-varying microphysics induced by a wind-bubble environment (Kong et al. 2010) and the collision of internal shocks (Guidorzi et al. 2007).

To test the existence of a flare in GRB 220831A’s OIR counterpart, we describe the flare with a phenomenological smoothly broken

powerlaw (SBPL) of the form,

$$F(\nu, t) = A\nu^\beta \tau^{-\alpha_1} \left\{ \frac{1}{2} \left(1 + \tau^{1/\Delta} \right) \right\}^{(\alpha_1 - \alpha_2)\Delta} \quad (3)$$

where $\tau = (t - t_0)/(t_b - t_0)$, t_0 is the start time of the flare and Δ is the smoothness parameter for which we assume $\Delta = 0.1$. We simultaneously fit the SBPL and a forward shock model with `AFTERGLOWPY`, forcing a positive value for α_1 . Our priors for the forward shock are based off a fit to the OIR data without the observations between 1 and 3 days post-burst. This is because we interpret the data before 1 day post-burst and after 3 days post-burst to be dominated by the forward shock and those between 1 and 3 days to be dominated by a separate emission mechanism based off the results of the empirical fit in Section 3.3.1 forward shock fit in Section 3.3.2.

The forward shock fit assumes $\epsilon_e = \epsilon_B = 0.1$ as they are consistent with our fit to the multi-wavelength data in Table 4 and, without fitting multi-wavelength data, these parameters are unconstrained. We also assume that the flare has a spectral index of $\beta = -0.69$, consistent with the BPL fit to the OIR afterglow. The data available is insufficient to constrain a change in the spectral energy distribution. We also cannot constrain the secondary emission component's effects on the X-ray and radio observations due to the lack of sampling. In this case, we therefore only fit to the OIR data to avoid making assumptions about secondary emission component's behaviour in other wavelengths.

The parameters of the resultant forward shock and flare are presented in Table 4 and 5 respectively and the light curve is shown in the central panel in Figure 8. Compared to a simple forward shock fit to the OIR data, we find moderate evidence for a flare with $\log_{10} \text{BF} = 0.96 \pm 0.07$, where BF is the Bayes factor. We also note that, with the median of the posterior distribution, plotted in Figure 8, there are still significant residuals, particularly with the *i*-band detections between 1 and 3 d post-burst.

3.4.4 Internal plateau

A significant fraction of both SGRB and LGRB X-ray afterglows have a plateau phase, where the decay of the light curve slows for a period of time before returning to a standard afterglow decay (Nousek et al. 2006). There are multiple interpretations for these external plateaus including energy injection into the forward shock from continued central engine activity (Bernardini et al. 2012; Rowlinson et al. 2014) and the result of angular structure in the jet (Eichler & Granot 2006; Oganessyan et al. 2020; Beniamini et al. 2020a).

X-ray afterglows can also exhibit an ‘internal plateau’ (Zhang et al. 2006; Liang et al. 2006), characterised by an extremely rapid decay in luminosity, such as observed, for example, from GRB 070110 (Troja et al. 2007; Beniamini & Mochkovitch 2017). Internal plateaus have also been proposed as explanation for the properties of the optical afterglows of GRBs 060605 and 080413B (Li et al. 2012), though the evidence for a steep decay is not required by the data (e.g., Ferrero et al. 2009).

The most popular of the proposed mechanisms to produce these internal plateaus is the presence of a long-lived millisecond magnetar central engine which spins down and eventually dissipates its energy by collapsing into a black hole (Lyons et al. 2010; Rowlinson et al. 2010; Zhang 2014). This process would be unlikely to produce an OIR plateau. However, not all explanations require a long-lived central engine. Another possible explanation proposed by Beniamini & Mochkovitch (2017) is photospheric emission arising from a moderately relativistic outflow (bulk Lorentz factor $\Gamma \lesssim 20$) launched by the central engine (e.g., a black hole or magnetar) at a similar time as the

highly relativistic material ($\Gamma \gtrsim 100$) producing the forward shock. However, in this photospheric emission scenario it is still difficult to produce the OIR emission (see Beniamini & Mochkovitch 2017, for details).

Whilst the steep decay after the temporal break in GRB 220831A's OIR counterpart is similar to what is observed in internal plateaus. To assess the possibility of an internal plateau in GRB 220831A's OIR light curve, we use a similar procedure as in Section 3.4.3. We conduct a joint fit with a forward shock and a phenomenological SBPL, restricting $\alpha_1 < 0$ and $t_0 = 0$. The resultant forward shock and SBPL parameters are shown in Tables 4 and 5 respectively and the best-fit light curve is presented in the right panel of Figure 8. As expected, we obtain a comparatively steep post-break powerlaw index where $\alpha_1/\alpha_2 = (7.5^{+9.2}_{-5.2}) \times 10^{-2}$. This is typical of an internal plateau observed in X-rays (e.g., Zhang et al. 2016; Troja et al. 2007; Rowlinson et al. 2010) and is similar to the suspected OIR internal plateaus present in GRBs 060605 and 080413B (Li et al. 2012). With this fit, we find $\log_{10} \text{BF} = 2.05 \pm 0.07$, constituting strong evidence in comparison to a simple forward shock. We note that the lower number of free parameters and its contribution to the flux of the $t < 1$ d observations would naturally give it a larger Bayes factor than the flare explanation. With the best-fit parameters presented in Table 5, we calculate a lower limit on the isotropic-equivalent energy release of the internal plateau of $> 10^{50}$ erg.

4 DISCUSSION

4.1 The origin of GRB 220831A

With the available data, we cannot assign a progenitor to GRB 220831A. The attempts to identify GRB 220831A's host galaxy and our study of its prompt emission have left the progenitor uncertain, with either a collapsar or a merger scenario open. The narrow jet opening angle and low circumburst density we infer in Table 4 weakly favours a SGRB (Fong et al. 2015; O'Connor et al. 2020). However, there is an overlap in the circumburst densities (e.g., Nysewander et al. 2009) and opening angles (e.g., Wang et al. 2018; Rouco Escorial et al. 2022) among LGRBs and SGRBs. We also acknowledge that the circumburst density measurements may be affected by the triple degeneracy in $E_{K, \text{iso}}$, n_0 and ϵ_B that exists for bursts observed at $\nu_m < \nu < \nu_c$ (e.g., Garcia-Cifuentes et al. 2024; Sfaradi et al. 2024).

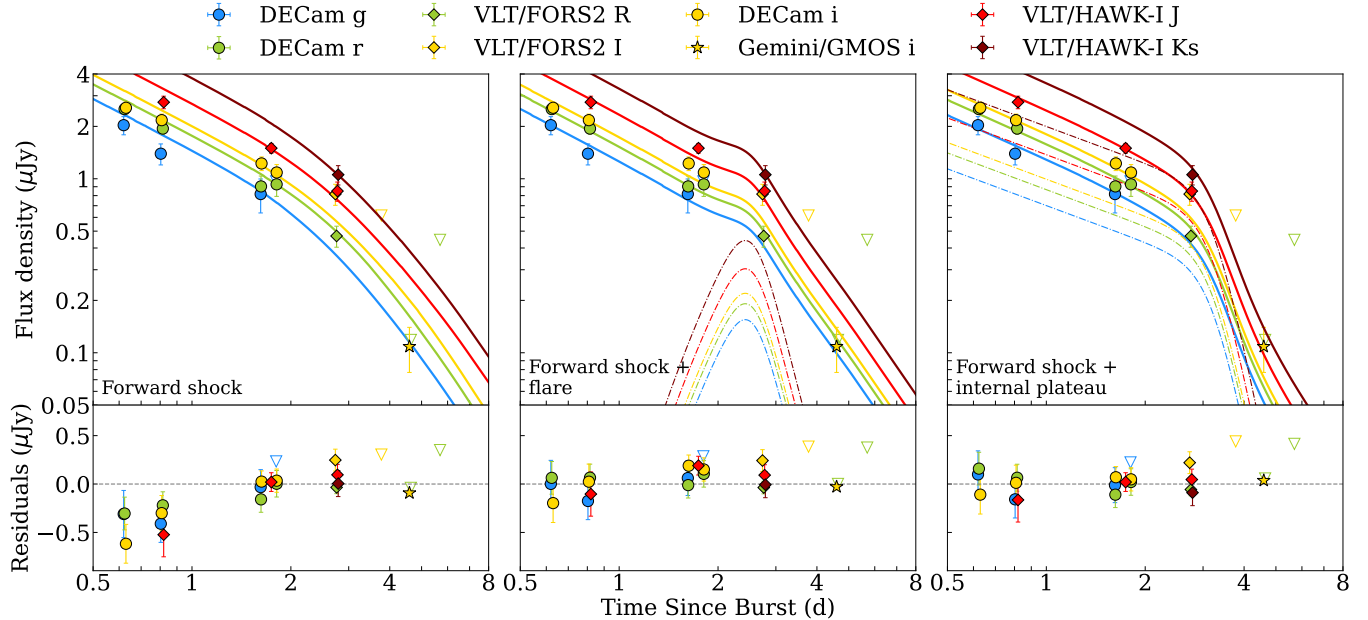
Due to the lack of a significant association with any nearby galaxies (Figure 2), we favour a high-*z* collapsar as the progenitor for GRB 220831A. This is also supported by the lack of a SN detection, which favours a distant origin at $z > 0.86$. Detecting a host galaxy for GRB 220831A at $z = 2.4$, would require a deep image with an upper-limit $m > 27.2$ AB mag which would correspond to $M > -18$ (Schulze et al. 2015). This is achievable with current 8-10 m class ground-based and space-based facilities, which may be required to detect the host galaxy and determine its redshift.

For future similar bursts, conducting rapid follow-up spectroscopy of their afterglow can yield a redshift measurement from absorption lines (e.g., de Ugarte Postigo et al. 2014; Agúf Fernández et al. 2023) and aid in the identification of a host galaxy and progenitor. This is a significant challenge for SGRBs due to the comparative rarity of a bright OIR afterglow and their rapid fade rate, often fading below the spectroscopic detection threshold before a day post-burst.

For distinguishing merger-driven GRBs from collapsar-driven GRBs, the detection of SNe and KNe accompanying intermediate-class GRBs like GRB 220831A can help understand the overlap between the populations of LGRBs and SGRBs. Additionally, by conducting high-cadence searches for OIR afterglows (e.g., Ho et al.

Table 5. Internal plateau and flare parameter estimations for fits to GRB 220831A’s afterglow assuming $z = 2.4$.

Fit	A $\log_{10} \mu\text{Jy}$	t_0 d	t_b d	α_1	α_2	$\log_{10} \text{BF}$
Forward shock + flare	$9.38^{+0.45}_{-2.59}$	$0.68^{+0.63}_{-0.47}$	$2.56^{+0.90}_{-0.42}$	$2.78^{+4.43}_{-2.21}$	$-6.16^{+2.88}_{-2.64}$	0.96 ± 0.07
Forward shock + internal plateau	$9.44^{+0.22}_{-0.19}$	0	$3.21^{+0.51}_{-0.38}$	$-0.70^{+0.39}_{-0.21}$	$-9.36^{+3.96}_{-3.76}$	2.05 ± 0.07

**Figure 8.** AFTERGLOWPY fits to GRB 220831A’s OIR afterglow with additional emission components. The solid lines denote the best-fit model, including both the forward shock and additional emission components. The dotted lines denote just the additional emission component. The left-hand panel shows just forward shock emission, the central panel shows a flare, described by a SBPL starting at some time post-burst and the right-hand panel shows an internal plateau described by a BPL starting at the time of burst. The best-fit parameters are listed in Tables 4 and 5.

2022; Freeburn et al. 2024) and the discovery of soft X-ray afterglows with facilities like *Einstein Probe* (Yuan et al. 2015, 2022) can help understand the diversity, rate and angular structure of successful jets originating from BNS mergers and collapsars. These data would aid in tying emission properties to specific progenitors.

4.2 GRB 220831A’s unusual afterglow

We observe departures from the standard forward shock closure relations in GRB 220831A’s OIR afterglow at a few days after the burst (see Figure 8). We uncover strong evidence for an additional emission component which may be either a flare or internal plateau on top of the forward shock, based on the phenomenological SBPL fits we conducted. However, the sampling of the light curve between 1 and 4 days post-burst is insufficient to discern the exact emission mechanism of the OIR excess.

As mentioned in Section 3.4, there is evidence for internal plateau emission in the optical afterglows to GRBs 060605 and 080413B (Li et al. 2012). GRB 060605’s temporal powerlaw indices are shown in Figure 6 and exhibits a similar steepening in its evolution, albeit at earlier times, with a break ~ 0.2 d post-burst compared with GRB 220831A’s ~ 3 d post-burst. GRB 060605’s high

redshift ($z = 3.78$) means that this steepening is occurring very early in its rest frame evolution. However, at $z = 1.1$, GRB 080413B has its temporal break at ~ 1 d post-burst (rest frame), a similar timescale to GRB 220831A, if it is $z \gtrsim 2$. However, Filgas et al. (2011) show that GRB 080413B’s optical afterglow is consistent with a two-component jet model, whereas the OIR counterpart to GRB 220831A’s post-break powerlaw index is too steep for this prescription.

Furthermore, the short ($T_{90} < 2$ s) duration of GRB 220831A presents a problem for the magnetar interpretation as a newly formed magnetar central engine would require > 10 s to impart an outflow with a large enough energy per baryon to produce a highly relativistic GRB (Beniamini et al. 2017). This problem can be mitigated, assuming a collapsar origin for GRB 220831A, by requiring the time for the jet to break out of the stellar envelope to be ~ 10 s before quickly shutting off. However, this scenario is statistically fine tuned and would require more evidence for us to favour it. Moreover, we note that it is not obvious from a theoretical perspective that an OIR internal plateau can be easily produced using the current theories. Through this lens, a delayed flare, originating from an internal process, is better explanation for our observations.

Consistent optical, hours-timescale cadence between 1 and 4 days

post-burst would have better constrained the presence of a flare activity against an internal plateau by sampling its rise in brightness. For bright OIR afterglows coordinated follow-up efforts by global telescope arrays such as the Gravitational Wave Optical Transient Observer (GOTO; Gompertz et al. 2020), the Las Cumbres Observatory (Brown et al. 2013), the Global Rapid Advanced Network Devoted to the Multi-messenger Addicts (GRANDMA; Antier et al. 2020a,b) and Global Relay of Observatories Watching Transients Happen (GROWTH; Kasliwal et al. 2019), among others, would aid in characterising brighter analogues of GRB 220831A.

5 CONCLUSIONS

The bimodal distribution of GRBs, comprising both short-hard and long-soft GRBs has typically been interpreted as being driven by binary neutron star mergers and collapsars respectively. In recent years, observations of kilonovae associated with long-soft GRBs have shown the shortcomings of this assumption. Exploring the parameter space between these two distributions may aid in constraining the fraction of collapsars in the short-hard regime and vice-versa.

In this work, we show that GRB 220831A was an intermediate class GRB which shows a significant departure from a typical forward shock dominated afterglow. We find that GRB 220831A is observationally hostless which indicates that it is either a high redshift collapsar or a low redshift binary neutron star merger with a large angular offset from its host. We favour a high- z collapsar as the origin for GRB 220831A due to *i*) the prompt emission's comparative softness, *ii*) its location on the Amati relation, *iii*) the lack of significant association with nearby galaxies and *iv*) the non-detection of an accompanying supernova or kilonova.

We fit two models to GRB 220831A's optical and near-infrared (OIR) counterpart, simulating a forward shock with both a delayed OIR flare and an OIR internal plateau, respectively. We find that the addition of the phenomenological models allows us to fit the data better than a forward shock on its own. However, the cadence of the OIR data is too slow to confirm the presence of an optical internal plateau over a flare or other additional emission mechanism.

For future GRB observations, we highlight the benefit of conducting rapid spectroscopic follow-up to obtain a redshift as it will allow for an easier determination of the event's progenitor. We also identify the opportunity, by conducting high-cadence observations (e.g., hour cadence) of GRB OIR afterglows out to a few days post-burst, to constrain phenomena like central engine activity and long-lived magnetars.

ACKNOWLEDGEMENTS

We thank Kathleen Labrie and the *Gemini* External Helpdesk for helpful discussions regarding *Gemini*/FLAMINGOS-2 data.

B.O. is supported by the McWilliams Postdoctoral Fellowship at Carnegie Mellon University.

JC acknowledges funding by the Australian Research Council Discovery Project, DP200102102.

A.M. is supported by the Australian Research Council DE230100055.

A.C.G. and the Fong Group at Northwestern acknowledges support by the National Science Foundation under grant Nos. AST-1909358, AST-2308182 and CAREER grant No. AST-2047919. A.C.G. acknowledges support from NSF grants AST-1911140, AST-1910471

and AST-2206490 as a member of the Fast and Fortunate for FRB Follow-up team.

Parts of this research were conducted by the Australian Research Council Centre of Excellence for Gravitational Wave Discovery (OzGrav), through project numbers CE170100004 and CE230100016.

Research at Perimeter Institute is supported in part by the Government of Canada through the Department of Innovation, Science and Economic Development and by the Province of Ontario through the Ministry of Colleges and Universities

This work was supported by the European Research Council through the Consolidator grant BHianca (grant agreement ID 101002761) and by the National Science Foundation (under award number 12850).

Parts of this work was performed on the OzSTAR national facility at Swinburne University of Technology. The OzSTAR program receives funding in part from the Astronomy National Collaborative Research Infrastructure Strategy (NCRIS) allocation provided by the Australian Government, and from the Victorian Higher Education State Investment Fund (VHESIF) provided by the Victorian Government.

This work made use of data supplied by the UK *Swift* Science Data Centre at the University of Leicester. Based on observations obtained at the international Gemini Observatory, a program of NSF's OIR Lab, which is managed by the Association of Universities for Research in Astronomy (AURA) under a cooperative agreement with the National Science Foundation on behalf of the Gemini Observatory partnership: the National Science Foundation (United States), National Research Council (Canada), Agencia Nacional de Investigación y Desarrollo (Chile), Ministerio de Ciencia, Tecnología e Innovación (Argentina), Ministério da Ciência, Tecnologia, Inovações e Comunicações (Brazil), and Korea Astronomy and Space Science Institute (Republic of Korea). Additionally, this work is based on data obtained from the ESO Science Archive Facility.

This research made use of MATPLOTLIB, a Python library for publication quality graphics (Hunter 2007), SCIPY (Virtanen et al. 2020), ASTROPY, a community-developed core Python package for Astronomy (Astropy Collaboration et al. 2013, 2018) and SCIKIT-LEARN (Pedregosa et al. 2011).

DATA AVAILABILITY

The majority of the data used for this work is publicly available on data archives. The data still in its proprietary period will be supplied upon reasonable request to the authors.

REFERENCES

- Abbott B. P., et al., 2017, *ApJ*, 848, L12
 Abbott T. M. C., et al., 2021, *ApJS*, 255, 20
 Agüí Fernández J. F., et al., 2023, *MNRAS*, 520, 613
 Ahumada T., et al., 2021, *Nature Astronomy*, 5, 917
 Amati L., 2006, *MNRAS*, 372, 233
 Amati L., et al., 2002, *A&A*, 390, 81
 Anderson G. E., et al., 2022, GRB Coordinates Network, 32529, 1
 Andreoni I., et al., 2017, *Publ. Astron. Soc. Australia*, 34, e069
 Antier S., et al., 2020a, *MNRAS*, 492, 3904
 Antier S., et al., 2020b, *MNRAS*, 497, 5518
 Arnaud K. A., 1996, in Jacoby G. H., Barnes J., eds, *Astronomical Society of the Pacific Conference Series Vol. 101, Astronomical Data Analysis Software and Systems V*. p. 17
 Ashton G., et al., 2019, *ApJS*, 241, 27
 Astropy Collaboration et al., 2013, *A&A*, 558, A33

- Astropy Collaboration et al., 2018, *AJ*, 156, 123
- Band D., et al., 1993, *ApJ*, 413, 281
- Barbary K., et al., 2024, *SNCosmo*, doi:10.5281/zenodo.592747
- Barnes J., Metzger B. D., 2023, *ApJ*, 947, 55
- Becerra R. L., et al., 2023, *MNRAS*, 522, 5204
- Behroozi P. S., Ramirez-Ruiz E., Fryer C. L., 2014, *ApJ*, 792, 123
- Beniamini P., Mochkovitch R., 2017, *A&A*, 605, A60
- Beniamini P., Piran T., 2024, *ApJ*, 966, 17
- Beniamini P., Giannios D., Metzger B. D., 2017, *MNRAS*, 472, 3058
- Beniamini P., Hotokezaka K., van der Horst A., Kouveliotou C., 2019, *MNRAS*, 487, 1426
- Beniamini P., Duque R., Daigne F., Mochkovitch R., 2020a, *MNRAS*, 492, 2847
- Beniamini P., Granot J., Gill R., 2020b, *MNRAS*, 493, 3521
- Beniamini P., Gill R., Granot J., 2022, *MNRAS*, 515, 555
- Berger E., 2010, *ApJ*, 722, 1946
- Bernardini M. G., Margutti R., Mao J., Zaninoni E., Chincarini G., 2012, *A&A*, 539, A3
- Bertin E., 2010, SWarp: Resampling and Co-adding FITS Images Together, Astrophysics Source Code Library, record ascl:1010.068
- Bertin E., Arnouts S., 1996, *A&AS*, 117, 393
- Bloom J. S., Kulkarni S. R., Djorgovski S. G., 2002, *AJ*, 123, 1111
- Bromberg O., Nakar E., Piran T., Sari R., 2012, *ApJ*, 749, 110
- Bromberg O., Nakar E., Piran T., Sari R., 2013, *ApJ*, 764, 179
- Brown T. M., et al., 2013, *PASP*, 125, 1031
- Burrows D. N., et al., 2005, *Science*, 309, 1833
- Cano Z., Wang S.-Q., Dai Z.-G., Wu X.-F., 2017, *Advances in Astronomy*, 2017, 8929054
- Colpi M., Geppert U., Page D., 2000, *ApJ*, 529, L29
- Covino S., et al., 2017, *Nature Astronomy*, 1, 791
- D'Avanzo P., Rossi A., Malessani D. B., Campana S., Levan A. J., Stargate Collaboration 2022, GRB Coordinates Network, 32513, 1
- Dai Z. G., Wang X. Y., Wu X. F., Zhang B., 2006, *Science*, 311, 1127
- Dichiara S., et al., 2021, *ApJ*, 911, L28
- Dichiara S., et al., 2022, GRB Coordinates Network, 32510, 1
- Dichiara S., Tsang D., Troja E., Neill D., Norris J. P., Yang Y. H., 2023, *ApJ*, 954, L29
- Dobie D., Kaplan D. L., Hotokezaka K., Murphy T., Deller A., Hallinan G., Nissanke S., 2020, *MNRAS*, 494, 2449
- Duque R., Beniamini P., Daigne F., Mochkovitch R., 2022, *MNRAS*, 513, 951
- Eichler D., Granot J., 2006, *ApJ*, 641, L5
- Eichler D., Livio M., Piran T., Schramm D. N., 1989, *Nature*, 340, 126
- Evans P. A., et al., 2014, *ApJS*, 210, 8
- Evans P. A., et al., 2017, *Science*, 358, 1565
- Evans P. A., et al., 2020, *ApJS*, 247, 54
- Evans P. A., Page K. L., Beardmore A. P., Eyles-Ferris R. A. J., Osborne J. P., Campana S., Kennea J. A., Cenko S. B., 2023, *MNRAS*, 518, 174
- Falcone A. D., et al., 2006, *ApJ*, 641, 1010
- Ferrero P., et al., 2009, *A&A*, 497, 729
- Filgas R., et al., 2011, *A&A*, 526, A113
- Fong W., Berger E., 2013, *ApJ*, 776, 18
- Fong W., et al., 2013, *ApJ*, 769, 56
- Fong W., Berger E., Margutti R., Zauderer B. A., 2015, *ApJ*, 815, 102
- Fong W.-f., et al., 2022, *ApJ*, 940, 56
- Foreman-Mackey D., Hogg D. W., Lang D., Goodman J., 2013, *PASP*, 125, 306
- Freeburn J., van Bemmell N., Dobie D., Moller A., Cooke J., Suhr M., 2022a, GRB Coordinates Network, 32516, 1
- Freeburn J., van Bemmell N., Dobie D., Moller A., Cooke J., Suhr M., Webb S., 2022b, GRB Coordinates Network, 32548, 1
- Freeburn J., et al., 2024, *MNRAS*, 531, 4836
- Fruchter A. S., et al., 2006, *Nature*, 441, 463
- Galama T. J., et al., 1998, *Nature*, 395, 670
- Garcia-Cifuentes K., Becerra R. L., De Colle F., Vargas F., 2024, *MNRAS*, 527, 6752
- Gehrels N., et al., 2004, *ApJ*, 611, 1005
- Gehrels N., et al., 2005, *Nature*, 437, 851
- Gillanders J. H., et al., 2023, *arXiv e-prints*, p. arXiv:2308.00633
- Goldstein A., Cleveland W. H., Kocevski D., 2023, Fermi Gamma-ray Data Tools: v2.0.0, <https://github.com/USRA-STI/gdt-fermi>
- Golenetskii S. V., Mazets E. P., Aptekar R. L., Ilinskii V. N., 1983, *Nature*, 306, 451
- Gompertz B. P., et al., 2020, *MNRAS*, 497, 726
- Gompertz B. P., et al., 2023, *Nature Astronomy*, 7, 67
- Gordon A. C., Tejos N., Kilpatrick C. D., 2022, GRB Coordinates Network, 32535, 1
- Granot J., Sari R., 2002, *ApJ*, 568, 820
- Guidorzi C., et al., 2007, *A&A*, 474, 793
- Guiriec S., et al., 2013, *ApJ*, 770, 32
- Hearsc 2014, HEASoft: Unified Release of FTOOLS and XANADU, Astrophysics Source Code Library, record ascl:1408.004
- Hjorth J., 2013, *Philosophical Transactions of the Royal Society of London Series A*, 371, 20120275
- Hjorth J., et al., 2003, *Nature*, 423, 847
- Ho A. Y. Q., et al., 2022, *ApJ*, 938, 85
- Hunter J. D., 2007, *Computing in Science and Engineering*, 9, 90
- Jakobsson P., et al., 2006, *A&A*, 447, 897
- Karachentsev I. D., Kashibadze O. G., 2006, *Astrophysics*, 49, 3
- Kasliwal M. M., et al., 2019, *PASP*, 131, 038003
- Kaspi V. M., Beloborodov A. M., 2017, *ARA&A*, 55, 261
- Klingler N. J., 2022, GRB Coordinates Network, 32521, 1
- Kong S. W., Wong A. Y. L., Huang Y. F., Cheng K. S., 2010, *MNRAS*, 402, 409
- Kouveliotou C., Meegan C. A., Fishman G. J., Bhat N. P., Briggs M. S., Koshut T. M., Paciesas W. S., Pendleton G. N., 1993, *ApJ*, 413, L101
- Krühler T., et al., 2015, *A&A*, 581, A125
- Kumar P., Panaitescu A., 2000, *ApJ*, 541, L51
- Leibler C. N., Berger E., 2010, *ApJ*, 725, 1202
- Levan A., et al., 2005, *ApJ*, 624, 880
- Levan A. J., et al., 2024, *Nature*, 626, 737
- Li L., et al., 2012, *ApJ*, 758, 27
- Liang E.-W., Zhang B.-B., Stamatikos M., Zhang B., Norris J., Gehrels N., Zhang J., Dai Z. G., 2006, *ApJ*, 653, L81
- Lu W., McKee C. F., Mooley K. P., 2021, *MNRAS*, 507, 3672
- Lyons N., O'Brien P. T., Zhang B., Willingale R., Troja E., Starling R. L. C., 2010, *MNRAS*, 402, 705
- Marongiu M., et al., 2022, *A&A*, 658, A11
- Meegan C., et al., 2009, *ApJ*, 702, 791
- Mei A., et al., 2022, *Nature*, 612, 236
- Norris J. P., Bonnell J. T., 2006, *ApJ*, 643, 266
- Nousek J. A., et al., 2006, *ApJ*, 642, 389
- Nugent A. E., et al., 2022, *ApJ*, 940, 57
- Nysewander M., Fruchter A. S., Pe'er A., 2009, *ApJ*, 701, 824
- O'Connor B., Beniamini P., Kouveliotou C., 2020, *MNRAS*, 495, 4782
- O'Connor B., et al., 2022a, *MNRAS*, 515, 4890
- O'Connor B., Troja E., Dichiara S., 2022b, GRB Coordinates Network, 32542, 1
- Oganesyan G., Ascenzi S., Branchesi M., Salafia O. S., Dall'Osso S., Ghirlanda G., 2020, *ApJ*, 893, 88
- Paczyński B., 1998, *ApJ*, 494, L45
- Panaitescu A., Mészáros P., 1999, *ApJ*, 526, 707
- Pedregosa F., et al., 2011, *Journal of Machine Learning Research*, 12, 2825
- Perets H. B., Beniamini P., 2021, *MNRAS*, 503, 5997
- Perna R., Armitage P. J., Zhang B., 2006, *ApJ*, 636, L29
- Pian E., et al., 2017, *Nature*, 551, 67
- Planck Collaboration et al., 2020, *A&A*, 641, A6
- Poolakkil S., et al., 2021, *ApJ*, 913, 60
- Rastinejad J. C., et al., 2022, *Nature*, 612, 223
- Rhoads J. E., 1997, *ApJ*, 487, L1
- Romano P., et al., 2006, *A&A*, 450, 59
- Rossi A., et al., 2022, *ApJ*, 932, 1
- Rouco Escorial A., et al., 2022, *arXiv e-prints*, p. arXiv:2210.05695
- Rowlinson A., et al., 2010, *MNRAS*, 409, 531
- Rowlinson A., Gompertz B. P., Dainotti M., O'Brien P. T., Wijers R. A. M. J., van der Horst A. J., 2014, *MNRAS*, 443, 1779

- Ryan G., van Eerten H., Piro L., Troja E., 2020, *ApJ*, 896, 166
- Sari R., Piran T., Narayan R., 1998, *ApJ*, 497, L17
- Schulze S., et al., 2015, *ApJ*, 808, 73
- Sfaradi I., et al., 2024, *MNRAS*, 527, 7672
- Smartt S. J., et al., 2017, *Nature*, 551, 75
- Speagle J. S., 2020, *MNRAS*, 493, 3132
- Sun H., et al., 2023, *arXiv e-prints*, p. arXiv:2307.05689
- Swenson C. A., Roming P. W. A., 2014, *ApJ*, 788, 30
- Swenson C. A., Roming P. W. A., De Pasquale M., Oates S. R., 2013, *ApJ*, 774, 2
- Tanvir N. R., et al., 2017, *ApJ*, 848, L27
- Tohuvavohu A., Kennea J. A., DeLaunay J., Palmer D. M., Cenko S. B., Barthelmy S., 2020, *ApJ*, 900, 35
- Tohuvavohu A., Kennea J. A., DeLaunay J., Raman G., 2022, GRB Coordinates Network, 32506, 1
- Troja E., et al., 2007, *ApJ*, 665, 599
- Troja E., et al., 2022, *Nature*, 612, 228
- Tunncliffe R. L., et al., 2014, *MNRAS*, 437, 1495
- Virtanen P., et al., 2020, *Nature Methods*, 17, 261
- Wang X.-G., Zhang B., Liang E.-W., Lu R.-J., Lin D.-B., Li J., Li L., 2018, *ApJ*, 859, 160
- Wood J., Meegan C., Fermi GBM Team 2022, GRB Coordinates Network, 32511, 1
- Woosley S. E., 1993, *ApJ*, 405, 273
- Yang J., et al., 2022, *Nature*, 612, 232
- Yang Y.-H., et al., 2024, *Nature*, 626, 742
- Yuan W., et al., 2015, *arXiv e-prints*, p. arXiv:1506.07735
- Yuan W., Zhang C., Chen Y., Ling Z., 2022, in , Handbook of X-ray and Gamma-ray Astrophysics. p. 86, doi:10.1007/978-981-16-4544-0_151-1
- Zhang B., 2014, *ApJ*, 780, L21
- Zhang B., Fan Y. Z., Dyks J., Kobayashi S., Mészáros P., Burrows D. N., Nousek J. A., Gehrels N., 2006, *ApJ*, 642, 354
- Zhang B., et al., 2009, *ApJ*, 703, 1696
- Zhang Q., Huang Y. F., Zong H. S., 2016, *ApJ*, 823, 156
- Zhang B. B., et al., 2021, *Nature Astronomy*, 5, 911
- de Ugarte Postigo A., et al., 2014, *A&A*, 563, A62
- von Kienlin A., et al., 2020, *ApJ*, 893, 46

APPENDIX A: A PERSISTENT ARTEFACT IN FLAMINGOS-2 IMAGING

In Section 2, we report that some of the data collected with *Gemini*/FLAMINGOS-2 at 9, 10 and 52 d post-burst (PI: O’Connor, O’Connor et al. 2022b) with the *J* and *K_s* filters suffers from an unknown image artefact likely introduced in the data reduction process (Kathleen Labrie, private communication), though we did not identify its exact cause in the data. Here, we assess that the detections in these filters are likely an image artefact, or, if it is astrophysical, that it is not associated with GRB 220831A.

There are three reasons for this. Firstly, additional late-time *Gemini* observations in *J*-band, stacked between July 2023 and March 2024 also excluded this earlier detection as a host galaxy as they derive deeper, more sensitive limits, shown in Table 2.

Secondly, the *Gemini J* and *K_s*-band detections in question are spatially coincident with each other but offset from the rest of the OIR detections by $\sim 0.6''$ (Figure A1). Whilst this is a small offset if they were due to a host galaxy, compared to the VLT afterglow detections with the same filters, we calculated a high significance of $\sim 14\sigma$ for the deviation of the Gemini artefacts from GRB 220831A’s localization after correcting for the astrometric tie uncertainty between the images. Given that they are not due to a host galaxy, this deviation rules out the association of them to GRB 220831A as either an afterglow, kilonova, or supernova. Dust echoes, originating from a nearby GRB, could produce such a signature due to superluminal

motion (Lu et al. 2021). However, this would occur hundreds of days post-burst, which is a much longer timescale than our observations at 9, 10 and 52 d post-burst.

Lastly, near-simultaneous observations with VLT/HAWK-I of GRB 220831A occurred within one hour after the initial *Gemini*/FLAMINGOS-2 detection at ~ 9 d post-burst (Figure A1). To account for this non-detection, the source would likely have to fade by >0.4 AB mag in ~ 1 hr and subsequently rebrighten to account for the *Gemini J*-band detection the next night at 10 d post-burst. This would be extremely peculiar behaviour for a GRB afterglow, SN, KN or a dust echo.

APPENDIX B: AFTERGLOW MODELING ASSUMING A LOW REDSHIFT

In the main body of this work, we determined that GRB 220831A is likely a $z > 2$ collapsar based on the non-detection of a high significance host galaxy association, its location to the Amati relation, and upper-limits on SN emission. However, we cannot strictly rule out a $z < 0.4$ compact binary merger origin for GRB 220831A. In Sections 3.3.2 and 3.4, we fit the data with various models, assuming $z = 2.4$. Here, we provide fits, assuming the low- z merger scenario with $z = 0.2$. We note that while there is no obvious host galaxy associated to GRB 220831A, a candidate host G0 does have a photometric redshift consistent with this redshift range but the probability of chance coincidence does not imply a robust association.

Figure B1 shows the multi-wavelength light curve and AFTERGLOWPY fit to the multi-wavelength data. The issues in fitting the steep temporal break at about 3 days post-burst, discussed in Section 3.3.2, are still present regardless of whether GRB 220831A is at $z = 0.2$ or $z = 2.4$.

In Tables B1 and B2, we find lower values of $E_{K,iso}$ and lower values of χ_{red}^2 in for the OIR forward shock model and the forward shock and flare model. Beyond a change to the energetics of the secondary emission component, it does not change our interpretation of the departures from closure relations discussed in Section 4.

APPENDIX C: RESULTS OF AFTERGLOW MODELING

In Section 3, we fit multiple models to GRB 220831A’s multi-wavelength afterglow. Here we present the corner plots from these fits. This includes a forward shock fit to the entire multi-wavelength dataset in Figure C1 and a forward shock fit to just the OIR data (Figure C2) and including a flare (Figure C3) and an internal plateau (Figure C4).

This paper has been typeset from a $\text{\TeX}/\text{\LaTeX}$ file prepared by the author.

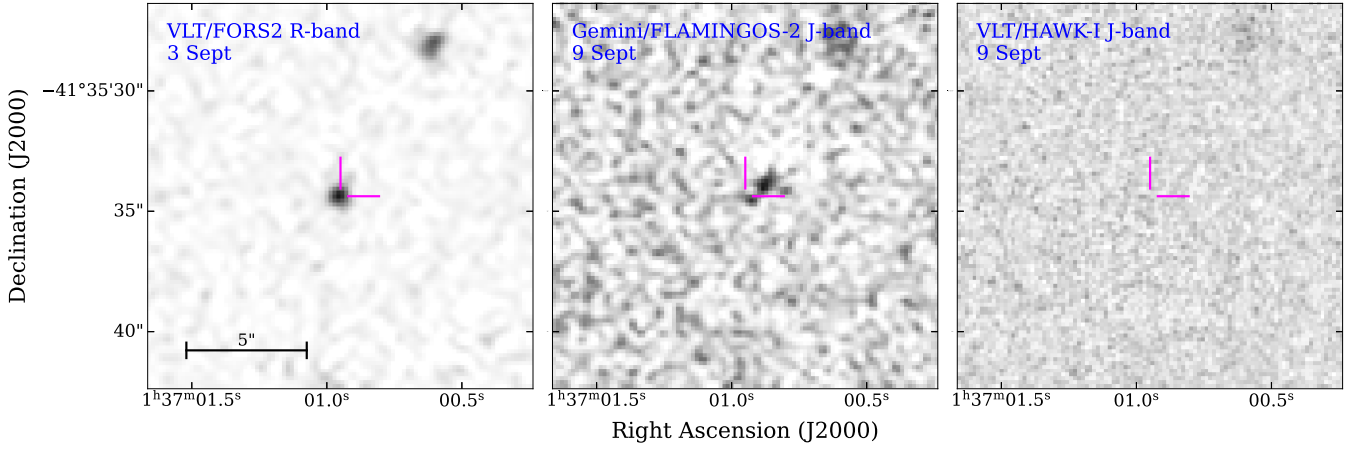


Figure A1. Images depicting the suspected image artefact in the *Gemini/FLAMINGOS-2* imaging. The left-hand panel shows the VLT/FORS2 *R*-band detection 3 September 2022, 2.7 d post-burst, the central panel shows the *Gemini/FLAMINGOS-2 J*-band ~ 24.5 AB mag detection of the suspected artefact, 9 d post-burst and the right-hand panel shows the near contemporaneous VLT/HAWK-I *J*-band non-detection which had a 5σ depth of > 24.9 AB mag. The images are not smoothed, but have been resampled with SWARP (Bertin 2010).

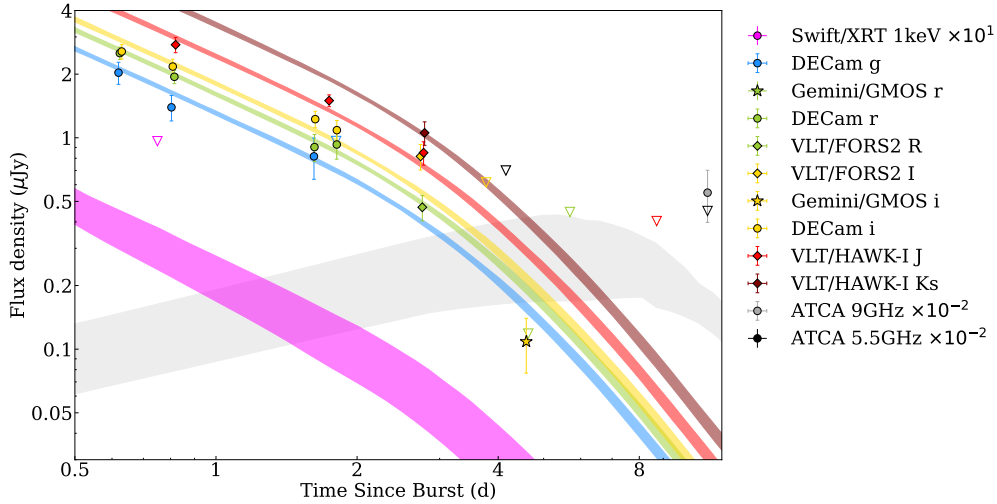


Figure B1. The light curve of GRB 220831A's afterglow. The solid lines denote the best-fit AFTERGLOWPY (Ryan et al. 2020) model, assuming $z = 0.2$. The shaded regions show the 1σ intervals for the fit. The X-ray and radio light curves have been rescaled for better readability.

Table B1. Forward shock parameter estimations from AFTERGLOWPY fits of GRB 220831A's afterglow assuming $z = 0.2$.

Data	Fit	$E_{K,iso}$ \log_{10} erg	n_0 \log_{10} cm $^{-3}$	θ_j rad	p	$\log_{10} \epsilon_e$	$\log_{10} \epsilon_B$	ϵ_γ	χ_{red}^2
All	Forward shock	$50.79^{+0.79}_{-0.76}$	$-3.06^{+1.22}_{-1.50}$	$0.12^{+0.09}_{-0.05}$	$2.27^{+0.06}_{-0.06}$	$-0.40^{+0.27}_{-0.36}$	$-1.29^{+0.93}_{-1.50}$	$0.08^{+0.32}_{-0.07}$	149.86
OIR	Forward shock	$50.86^{+0.64}_{-0.52}$	$-2.78^{+1.47}_{-1.78}$	$0.12^{+0.10}_{-0.06}$	$2.26^{+0.06}_{-0.06}$	-1	-1	$0.83^{+0.12}_{-0.38}$	2.08
OIR	Forward shock + flare	$51.09^{+0.09}_{-0.09}$	$-3.49^{+0.25}_{-0.24}$	$0.08^{+0.01}_{-0.01}$	$2.27^{+0.06}_{-0.05}$	-1	-1	$0.74^{+0.07}_{-0.11}$	1.43
OIR	Forward shock + internal plateau	$50.99^{+0.10}_{-0.11}$	$-3.63^{+0.28}_{-0.30}$	$0.08^{+0.01}_{-0.01}$	$2.26^{+0.07}_{-0.07}$	-1	-1	$0.78^{+0.07}_{-0.16}$	1.03

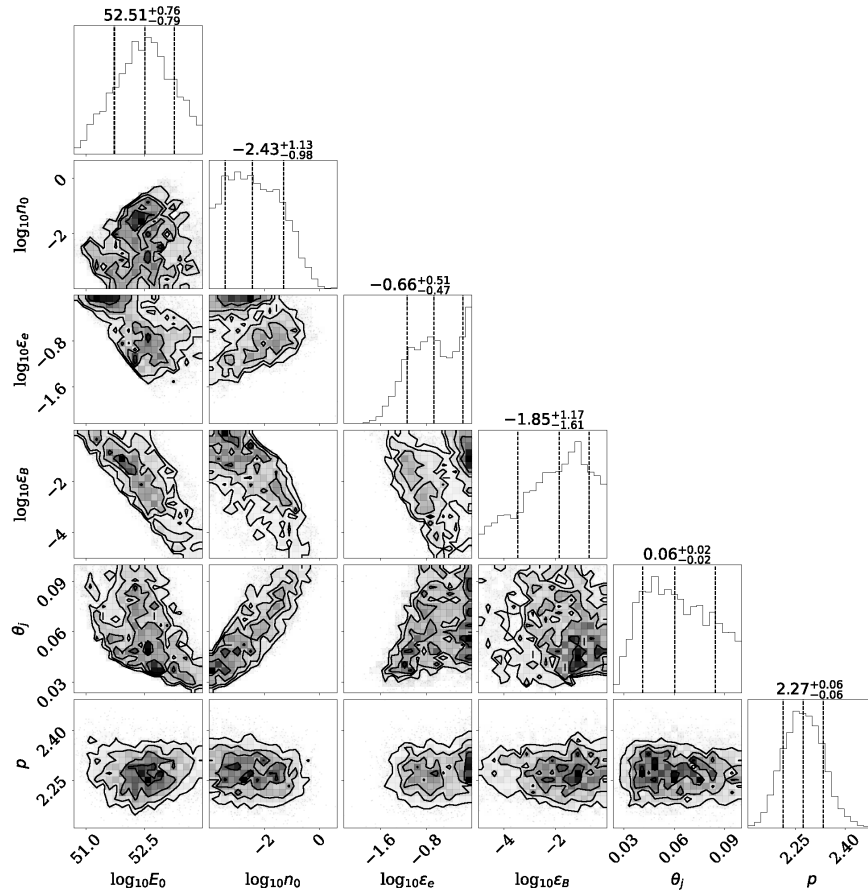


Figure C1. The corner plot corresponding to the multi-wavelength forward shock fit in Figure 4. We note the poor constraints on ϵ_e and ϵ_B which we attribute to the poor sampling of the X-ray and radio light curves. E_0 , n_0 and θ_j are in units of erg cm^{-3} and radians respectively.

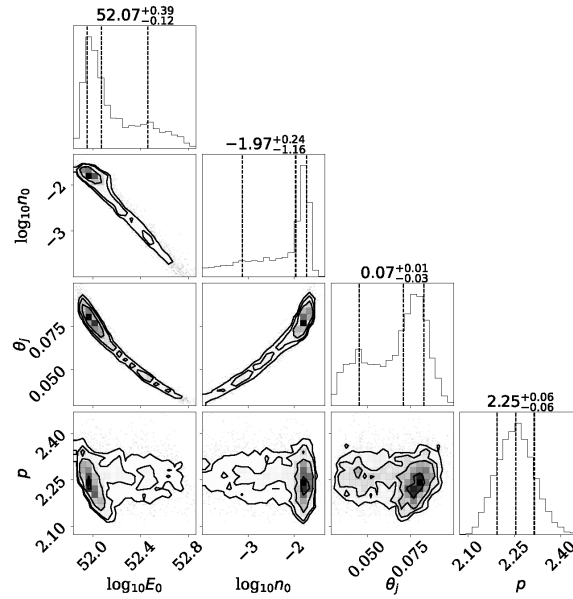
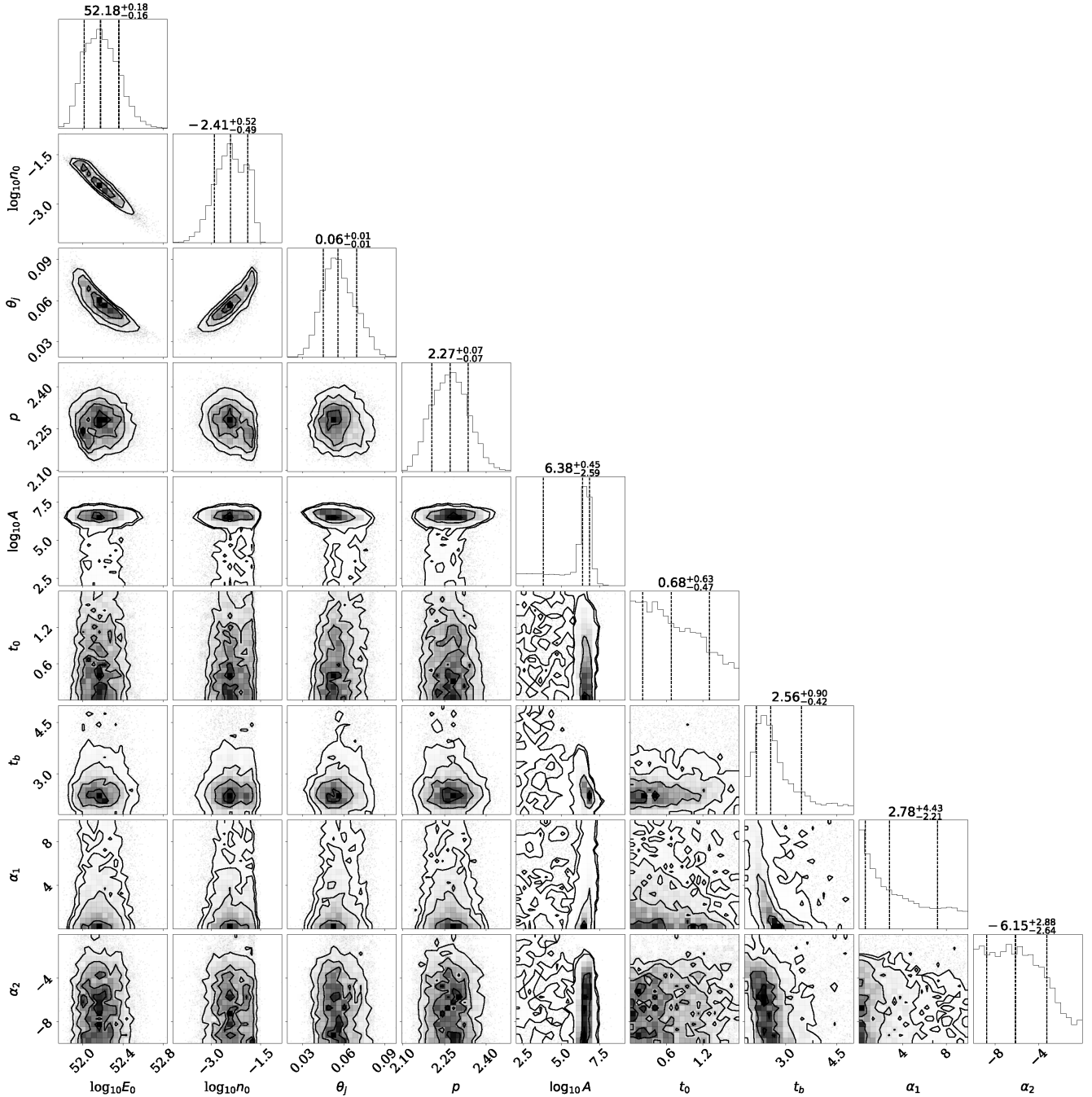


Figure C2. The corner plot corresponding to the forward shock fit in Figure 8.

Table B2. Internal plateau and flare parameter estimations for fits to GRB 220831A's afterglow assuming $z = 0.2$.

Fit	A $\log_{10} \mu\text{Jy}$	t_0 d	t_b d	α_1	α_2	$\log_{10} \text{BF}$
Forward shock + flare	$9.50^{+0.36}_{-1.72}$	$0.63^{+0.61}_{-0.45}$	$2.52^{+0.68}_{-0.37}$	$2.42^{+4.42}_{-1.94}$	$-6.28^{+2.81}_{-2.53}$	1.97 ± 0.07
Forward shock + internal plateau	$9.37^{+0.19}_{-0.18}$	0	$3.23^{+0.49}_{-0.39}$	$-0.49^{+0.32}_{-0.28}$	$-9.73^{+3.89}_{-3.53}$	2.05 ± 0.07

**Figure C3.** The corner plot corresponding to the forward shock and flare fit in Figure 8. A is in units of μJy and t_0 and t_b are in units of days.

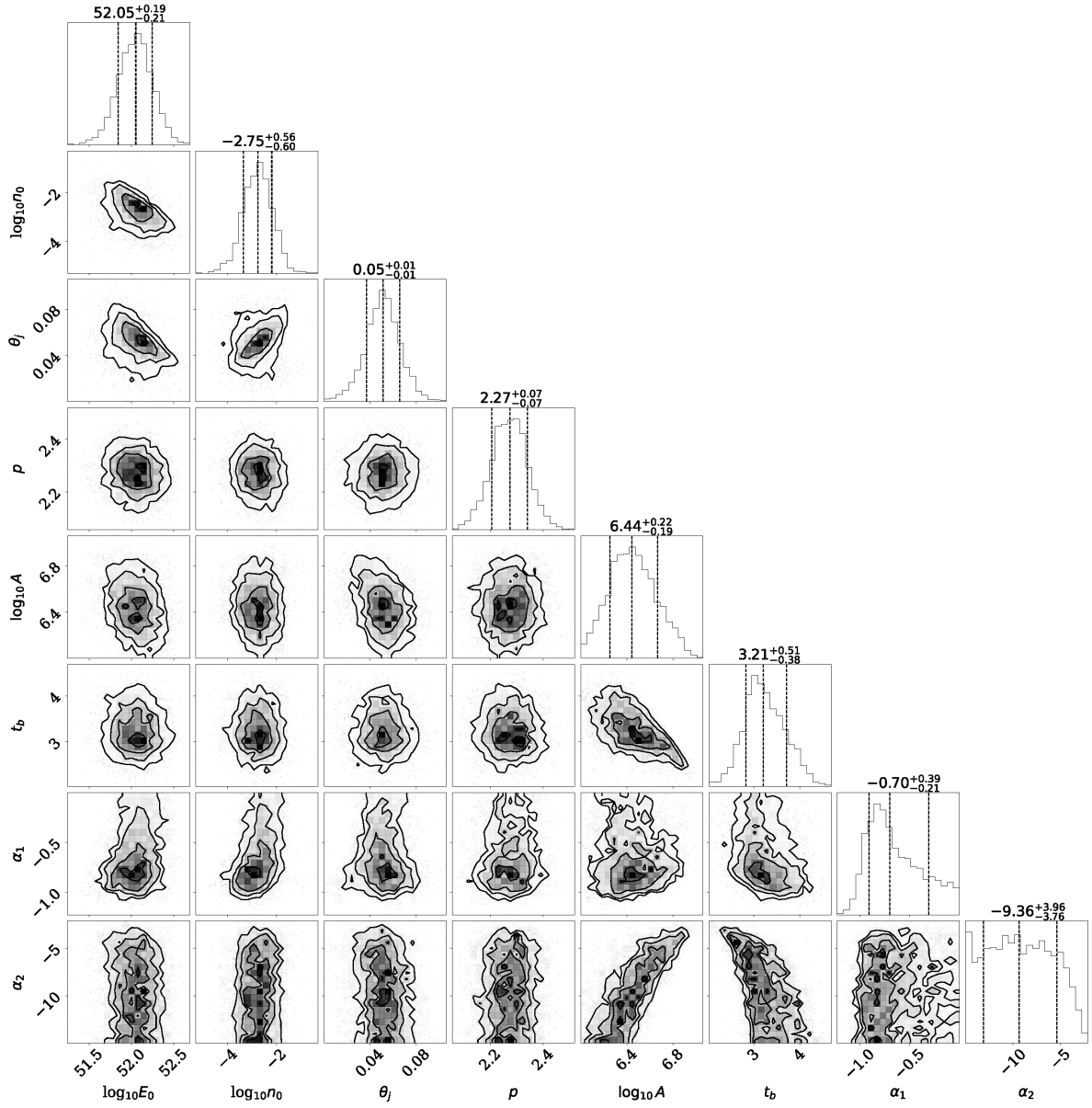


Figure C4. The corner plot corresponding to the forward shock and internal plateau fit in Figure 8.